Design of Chemoresponsive Liquid Crystals using Metal-Coordinating Polymer Surfaces

Nanqi Bao,[+] Tibor Szilvási,[#] Trevor Franklin,[+] Trenton J. Wolter,[#] Ayushi Tripathi,[+] Robert J. Twieg,[$] Rong Yang,[,+] Manos Mavrikakis,[*,#] Nicholas L. Abbott[*,+]*

[+]Smith School of Chemical and Biomolecular Engineering, Cornell University, Ithaca, NY 14853, USA

[#]Department of Chemical and Biological Engineering, University of Wisconsin-Madison, Madison, WI 53706, USA

[$]Department of Chemistry and Biochemistry, Kent State University, 1175 Risman Drive, Kent, Ohio 44242, United States

KEYWORDS: liquid crystals, coordinating polymers, metal cations, interfaces

ABSTRACT

Liquid crystals (LCs), when interfaced with chemically functionalized surfaces, can amplify a range of chemical and physical transformations into optical outputs. While metal cation-binding sites on surfaces have been shown to provide a basis for the design of chemoresponsive LCs, the cations have been found to dissociate from the surfaces and dissolve slowly into LCs, resulting in time-dependent changes in the properties of LC-solid interfaces (which impacts the reliability of

devices incorporating such surfaces). Here, we explore the use of surfaces comprised of metal-coordinating polymers to minimize dissolution of metal cations into LCs, and characterize the impact of the interfacial environment created by the coordinating polymer on the ordering and time-dependent properties of LCs. In particular, by combining theoretical (electronic structure calculations) and experimental (polarization-modulation infrared reflection-adsorption spectroscopy) results, we determine that the pyridine groups of a thin film of poly(4-vinylpyridine-*co*-divinylbenzene) (P(4VP-*co*-DVB)) coordinate with Ni^{2+} when $Ni(ClO_4)_2$ is deposited onto the film. We provide evidence that the Ni^{2+}-pyridine coordination weakens the binding of Ni^{2+} with 4'-*n*-pentyl-4-biphenylcarbonitrile (5CB), a room-temperature nematic LC, as compared to $Ni(ClO_4)_2$ supported on glass, although binding is still sufficiently strong to induce a homeotropic (perpendicular) orientation of the LC. Exposure of the 5CB films supported on $Ni(ClO_4)_2$-decorated P(4VP-*co*-DVB) substrates to parts-per-million vapor concentrations of dimethylmethylphosphonate (DMMP) was found to trigger orientational transitions (to planar (parallel) orientations) in the LC films. In contrast, 5CB supported on $Ni(ClO_4)_2$-decorated glass surfaces exhibited no response, even though displacement of 5CB by DMMP is predicted by computations to be thermodynamically favored in both cases. We propose that the distinct LC responses measured on glass and the coordinating polymer substrates are governed by the kinetics of displacement of 5CB by DMMP, a proposal that is supported by measurements performed with increasing temperature. Importantly, by using Ni^{2+} supported on P(4VP-*co*-DVB), we measured the ordering of 5CB to be stable and long-lived (>7 days), in contrast to unstable LC ordering (<14 hours) when using Ni^{2+} supported on glass under dry conditions and at room temperature. We further demonstrate the stability of $Ni(ClO_4)_2$ supported on P(4VP-*co*-DVB) towards higher temperatures and humidity using E7 as the LC. Overall, these results demonstrate that metal-coordinating polymer films are a promising class of substrates with which to fabricate robust and long-lived chemoresponsive LCs.

INTRODUCTION

Chemically-responsive (chemoresponsive) materials[1,2] have broad potential applications, including as sensors,[3] actuators,[4] and for delivery of therapeutics.[5] Liquid crystals (LCs) provide the basis of a particularly promising class of chemoresponsive materials[6–17], as they are fluid phases within which the molecules (mesogens) exhibit long-range ordering that can be controlled by their chemical environment.[18,19] The responsiveness of LCs to chemical environments has been explored using a number of strategies, including (1) changes in the mesoscale organization of bulk LC phases (e.g., cholesteric LCs[20,21], liquid crystal droplets and emulsions[22–27] and chemically sensitive chiral dopants[28–36]) and (2) surface-induced changes in LC ordering[3,37–44] upon exposure to targeted chemical species. Here, we build on the second strategy motivated by the observation that LCs can be triggered to undergo ordering transitions in response to specific atomic-scale events at interfaces.[45,46]

One surface-based approach that has shown particular promise for the design of chemoresponsive LCs combines the use of surfaces that present metal ions with mesogens possessing ligands capable of coordinating with the metal ions.[3,47–49] The competitive binding of the mesogens and targeted chemical species (e.g., dimethylmethylphosphonate, DMMP) with the metal ions couples the ordering of the LC to the absence/presence of the targeted chemical species.[3] For example, previous experimental studies have demonstrated surface-driven ordering transitions (from homeotropic ordering to planar ordering) of 4'-*n*-pentyl-4-biphenylcarbonitrile (5CB, Scheme 1a) when DMMP vapors partition into LC thin films (~20 µm thick) supported on metal perchlorate salts (e.g., $Al(ClO_4)_3$, $Cu(ClO_4)_2$, and $Zn(ClO_4)_2$).[3,50–57] While a number of substrates (e.g., self-assembled monolayers[3,50,56–59] and glass microscope slides[37,52–55,60]) have been used to support the metal salts, the time-dependent dissolution of the metal salts into the LC has been observed to generate time-dependent changes in the ordering of the LC (e.g., loss of homeotropic ordering within 7-hours of equilibrium of 5CB on the $Al(ClO_4)_3$-coated surface[58]). To address this problem, here we explore the use of metal-coordinating polymer films as a class of supports for metal cations that prevent minimize dissolution of the metal cations into LCs and investigate the consequence of the coordinating interfacial environment on the ordering and time-dependent properties of the supported LCs.

Our approach was inspired by prior studies that have reported formation of coordination complexes between the nitrogen lone pairs on poly(4-vinylpyridine) (P4VP) and metal ions (e.g., Ni^{2+}, Cu^{2+}, Fe^{3+}, and Zn^{2+} in acetate salts).[61–65] To generate pyridine-containing thin-film substrates for chemoresponsive LCs, we utilized an all-dry synthesis technique called initiated Chemical Vapor Deposition (iCVD).[66] This technique deposits smooth, conformal films atop substrates of interest,[67] and can be performed with a range of methacrylate- or vinyl-based monomers to enable precise control of the composition and physicochemical properties of polymer films.[68] Fabrication of P4VP thin films by iCVD has been previously reported,[69–72] and incorporation of the crosslinker poly(divinylbenzene) (PDVB) was shown to permit tuning of mechanical strength[70] and glass transition temperature.[73] For the design of chemoresponsive LCs, we fabricated thin films (~200 nm thick) of poly(4-vinylpyridine-*co*-divinylbenzene) (P(4VP-*co*-DVB)) on glass microscope slides using iCVD and controlled the cross-linker, DVB, to be 18 mol%. This made pyridine the dominant chemical group (82 mol%) at the surface of the polymer film and led to desirable mechanical properties for metal salt coating (e.g., prevented surfaces from delamination during metal-salt coating using alcoholic solutions).

In this paper, we report the use of electronic structure-based theoretical methods[37,52–54,74–77] and experiments to explore (i) how the binding of metal cations with coordinating polymers modulates their interactions with LCs, including the displacement of LCs by other chemical species (i.e., DMMP); (ii) whether these influences can be understood in terms of thermodynamic or kinetic factors; and (iii) whether the interfacial environment of the metal-coordinating polymer exhibits time-independent properties in comparison to metal salts deposited onto glass substrates (silica).

METHODS

Computations

Density functional theory (DFT) calculations were performed using Gaussian09 version D.01.[78] Geometry optimization was carried out at the PBE-D3/def2-SVP level of theory.[79–81] Electronic energies were then obtained from a single-point calculation at the M06-2X-D3/def2-TZVP[82] level of theory using the optimized structures. Free energy contributions were obtained from the PBE-D3/def2-SVP level of theory using a pressure of 1 atm and a temperature of 298 K. We modeled $Ni(ClO_4)_2$ using the Neutral Anion Model (NAM), which we have described in detail and established as a good predictor of LC ordering on metal salts in previous publications.[37,52,53] Within the context of the NAM, $Ni(ClO_4)_2$ coordinated with hydroxylated silica (SiO_4H_4), pyridine or ethanol was used to represent the surface when the metal salt is coordinated with the glass slide, polymer film, or washed by ethanol, respectively. Hydroxylated silica was used so that the silicon atom has a similar coordination environment (4 oxygen atoms) to what it would have in the bulk structure, and the hydrogen atoms were added to balance the charges.

Binding free energies (G_{BE}) for adsorbate molecules were calculated using the equation $G_{BE} = G_{Model+Ads} - G_{Model} - G_{Ads}$, where $G_{Model+Ads}$ is the free energy of the adsorbate molecule bound to the cluster model of the surface (NAM + any coordinating molecules such as pyridine), G_{Model} is the free energy of the cluster model of the surface, and G_{Ads} is the free energy of the adsorbate molecule in the gas phase. We use benzonitrile (PhCN, Scheme 1b) as a surrogate molecule for 5CB.[55] In past studies, we have found that a negative G_{BE} of PhCN with a NAM cluster was a reliable predictor of homeotropic anchoring.[52,53] We calculate the displacement free energy (G_{DE}) of 5CB by DMMP using the equation $G_{DE} = G_{BE-DMMP} - G_{BE-LC}$, where $G_{BE-DMMP}$ is the binding free energy of DMMP with a NAM cluster model of the surface, and G_{BE-LC} is the binding free energy of PhCN with the same NAM cluster model.

Experimental Section

Materials. Detailed information regarding the sources of materials used in this study can be found in SI.

Synthesis of polymer thin films. A custom-built iCVD reactor was used to deposit polymer thin films onto glass slides, silicon (Si) wafers or gold (Au)-coated silicon wafers. Detailed information regarding procedures used for synthesis of the polymer thin films used in this study can be found in SI. The final polymer film thickness was measured on the Si wafer using a Woollam alpha-SE ellipsometer at incident angles of 65°, 70° and 75°. Measurements were collected using incident light with wavelengths ranging from 380 to 900 nm and analyzed using a Cauchy-Urbach model.[83] The copolymer compositions were determined by Fourier-transform infrared spectroscopy (Figure S3). The polymer thin films used in this study consisted of 82 mol% 4VP and 18 mol% DVB (see details in SI for other P(4VP-*co*-DVB) films with different 4VP-DVB ratios).

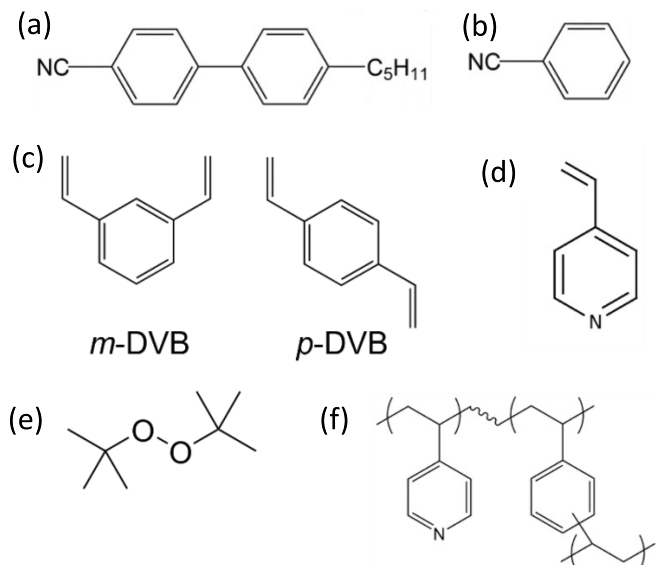

Scheme 1. Chemical structures of (a) 5CB, (b) PhCN, (c) DVB, (d) 4VP, (e) TBPO, (f) P(4VP-*co*-DVB).

Coating of metal salts on substrates. Glass slides or silicon wafers were rinsed with copious amounts of ethanol and then dried under a stream of nitrogen. P(4VP-*co*-DVB) thin films were deposited as described above. Metal ions were deposited onto glass surfaces or polymer thin film-coated glass substrates by spin coating ethanolic solutions of metal salts at specified molar concentrations (0.5-1.5 mM) at 3000 rpm for 30 s (WS-400A-6NPP/Lite, Laurell Technologies). The mole density of metal ions deposited on the glass surfaces or polymer films was quantified by using inductively coupled plasma-optical emission spectroscopy (ICP-OES), as detailed in SI.

Fourier transformed polarization-modulation infrared reflectance absorbance spectroscopy (PM-IRRAS). Substrates used in the IR measurements were prepared by sequential deposition of 20 Å of Ti and 200 Å of Au onto Si wafers using an electron beam evaporator. Films of P(4VP-*co*-DVB) (with thickness of 44 nm) were deposited on top of the Au films. IR spectra of the supported polymer films before and after being decorated with metal salts were obtained using a Nicolet Magna-IR 860 FT-IR spectrometer with a photoelastic modulator (PEM-90, Hinds Instruments), synchronous sampling demodulator (SSD-100), and a liquid N_2-cooled mercury cadmium telluride (MCT) detector. All spectra (700-4000 cm^{-1}) were recorded at an incident angle of 83° with the modulation centered at 1500 cm^{-1}. For each sample, 1000 scans were taken at a resolution of 4 cm^{-1}. Data were collected as differential reflectance vs. wavenumber. All IR results presented were analyzed by OMNIC software.

Formation of thin films of LC anchored on metal salt-decorated surfaces. An 18 μm-thick copper transmission electron microscopy (TEM) grid (Electron Microscopy Sciences) was placed on a metal salt-decorated surface. The TEM grid had an overall diameter of 3 mm and was composed of square slots with lateral dimensions of 285 μm. The slots were filled with 0.1 μL LC using a microcapillary. The excess LC was removed from the grids by wicking it into an empty capillary tube. In other experiments, the LC films were confined by two metal salt-decorated surfaces using a sandwich structure. Fiber spacers with diameters of 20 μm were dispersed into Norland Optical Adhesive 65 (Norland Products, Inc.). The perimeters of two surfaces were coated with the adhesive, and the surfaces were adhered together by UV exposure for 30 minutes. A drop of 5CB, heated into its isotropic phase (35.5 °C $<$ T $<$ 40 °C), was then drawn by capillarity into the cavity between the two surfaces of the sandwich cell. The cell was subsequently cooled to room temperature.

Characterization of orientations of LCs in an optical cell during gas exposure. LC samples hosted within TEM grids supported on metal salt-decorated glass or polymer surfaces were exposed to a stream of nitrogen containing 10 ppm DMMP within a flow cell that was constructed to direct the gaseous flow across the LC samples while permitting observation using a polarized-light microscope (CH40, Olympus). A detailed description of the flow cell can be found in a prior publication.[50] White light illumination was used to perform the microscopic observations. The flow rate of each gas stream was controlled using a rotameter (Aalborg Instruments and Control). The total flow rate was maintained at 500 mL/min at atmospheric pressure. Unless stated otherwise, the experiments were performed at room temperature (24^{o}C).

RESULTS AND DISCUSSION

Interactions of metal cations with coordinating polymer films

Previously, we reported experimental observations of homeotropic (perpendicular to the surface) anchoring of 4'-*n*-pentyl-4-biphenylcarbonitrile (5CB, a room-temperature LC) on $Ni(ClO_4)_2$-decorated glass surfaces.[52,74] These observations were correctly described by density functional theory (DFT), revealing strong binding (negative binding free energy) of the nitrile group in 5CB with Ni^{2+}. Motivated by these prior observations, in our initial experiment, we sought to use a poly(4-vinylpyridine-*co*-divinylbenzene) (P(4VP-*co*-DVB)) thin film as a substrate for coordination with Ni^{2+}. We evaluated the binding strength of 5CB with the Ni^{2+}-coordinating polymer film and compared it to Ni^{2+}-decorated glass surfaces using DFT calculations.

We first evaluated the binding free energy (G_{BE}) of $Ni(ClO_4)_2$ to P(4VP-*co*-DVB) or glass surfaces by performing calculations with $Ni(ClO_4)_2$ coordinated with pyridine or a hydroxylated silica cluster, respectively (see details in Methods and SI). We evaluated the formation energies of $Ni(ClO_4)_2$-pyridine complexes containing different numbers of the pyridine group (Figure S1) and found that the most thermodynamically stable structure is $Ni(ClO_4)_2$ coordinated with a single pyridine molecule (Figure 1a). Inspection of Figure 1a reveals that Ni^{2+} binds to the pyridine group more strongly (-1.44 eV) than to a hydroxylated silica cluster (-0.94 eV). The strong binding of Ni^{2+} with pyridine is consistent with prior experimental observations of the formation of Ni^{2+}-pyridine complexes in solution, which have been characterized by infrared (IR) spectroscopy.[84–86] To provide experimental characterization of the coordination of $Ni(ClO_4)_2$ with the pyridine group of P(4VP-*co*-DVB) films, we performed polarization-modulation infrared reflectance absorbance spectroscopy (PM-IRRAS).[87] Inspection of the IR spectrum of the bare P(4VP-*co*-DVB) (82 mol% 4VP and 18 mol% DVB) thin film (Figure 1b (red) with assignments of IR peaks in Table 1) reveals peaks corresponding to the vibrational modes of the pyridine group (1599, 1557, 1453, and 1415 cm^{-1}).[88] Next, we spin-coated $Ni(ClO_4)_2$ with a surface density of 8.2±0.4 $pmol/mm^2$ on the P(4VP-*co*-DVB) thin film. The surface density of 8.2±0.4 $pmol/mm^2$ is close to ~ 1 ML $Ni(ClO_4)_2$ salt coverage (8.4 $pmol/mm^2$ is 1 ML $Ni(ClO_4)_2$).[52] The black line in Figure 1b shows that additional IR peaks appear after $Ni(ClO_4)_2$ coating. Specifically, we observed the appearance of a broad peak at 1140-1070 cm^{-1} (marked with a diamond in Figure 1b), which is assigned as the vibrational mode of ClO_4^-.[89] The broad peak at 1670-1640 cm^{-1} and the peak at 1618 cm^{-1} (marked with asterisks in Figure 1b) are shifted relative to the C=N stretch of uncoordinated pyridine at 1599 cm^{-1}, and are weaker in intensity (from red to black at 1599 cm^{-1}). Comparable shifts to higher wavenumbers (>1610 cm^{-1}) for the C=N stretch of pyridine have been reported for complexes of P4VP with Zn^{2+} [84] and Ru^{2+}.[85,90] A similar set of observations and conclusions applies to the peak at 1415 cm^{-1} of the bare polymer and the peak at 1445 cm^{-1} of the $Ni(ClO_4)_2$-decorated polymer for the C=N stretch.[85] Overall, these results are consistent with the formation of Ni^{2+}-pyridine complexes, as reported in past studies,[85,86,90,91] and a strong coordination interaction of Ni^{2+} with pyridine, as predicted from our electronic structure calculations. We note also that our IR results suggest that uncoordinated pyridine remains on the surface after treatment with $Ni(ClO_4)_2$.

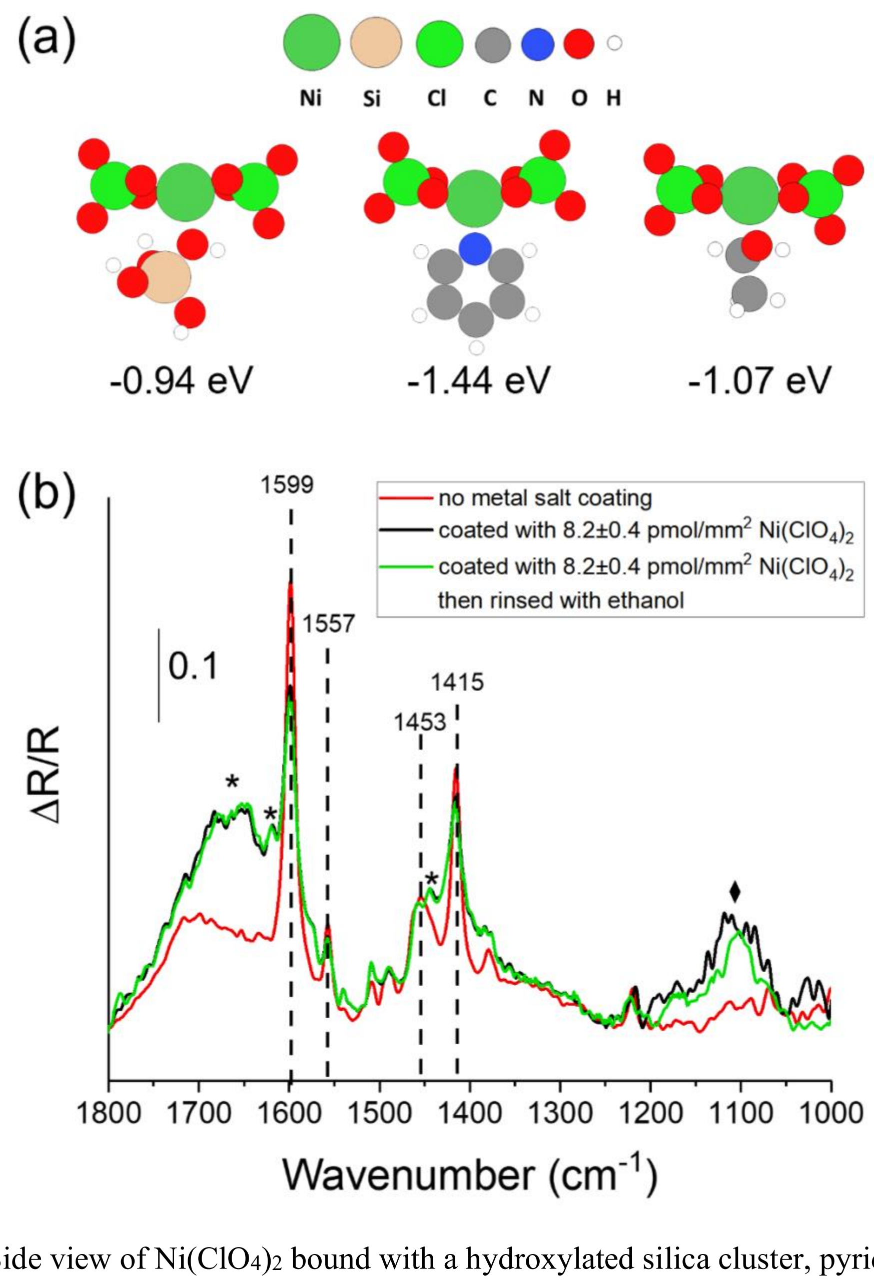

Figure 1. (a) Side view of $Ni(ClO_4)_2$ bound with a hydroxylated silica cluster, pyridine, or ethanol molecule (left to right). (b) PM-IRRAS of P(4VP-*co*-DVB) thin films before (red) and

after (black) being decorated with 8.2±0.4 pmol/mm^2 $Ni(ClO_4)_2$, and then being rinsed using ethanol (green). The characteristic IR peaks assigned for vibrational modes of the pyridine group coordinated with Ni^{2+} are marked above the peaks with asterisks, and the characteristic IR peak for the vibrational mode of ClO_4^- is marked above the peak with a diamond.

Table 1. Vibrational frequency (cm^{-1}) assignments for peaks in Figure 1b.

	pyridine ring				pyridine coordinated with Ni^{2+} (marked with asterisks)			ClO_4^- (marked with a diamond)
measured	1599	1557	1453	1415	1670-1640	1618	1445	1140-1070
reported[84,85,90,92]	1595	1556	1450	1415	>1610		1430	1200-1000
calculated	1595	1564	1495	1432	1620		1445	1098

Next, we evaluated the predicted (see calculations above) stronger binding of Ni^{2+} to pyridine (G_{BE}=-1.44 eV) than to hydroxylated silica (G_{BE}=-0.94 eV) by examining whether the Ni^{2+}-pyridine or Ni^{2+}-hydroxylated silica coordination can be disrupted by solvent such as ethanol. We calculated the G_{BE} of $Ni(ClO_4)_2$ to ethanol to be -1.07 eV (Figure 1a; less negative than -1.44 eV for the G_{BE} of Ni^{2+} to pyridine), leading us to predict that ethanol would not displace pyridine from binding to $Ni(ClO_4)_2$. We tested this prediction by measuring the IR spectra of the $Ni(ClO_4)_2$-decorated P(4VP-*co*-DVB) thin films before and after being rinsed with copious amounts of ethanol. Inspection of the green line in Figure 1b reveals no significant change in the spectra after ethanol rinsing, indicating that $Ni(ClO_4)_2$ remains coordinated with the polymer surface. In contrast to the coordinating polymer surface, the removal of $Ni(ClO_4)_2$ by ethanol is predicted on the glass surface (-0.94 eV for G_{BE} of Ni^{2+} to hydroxylated silica; less negative than -1.07 eV for the G_{BE} of Ni^{2+} to ethanol). As detailed in the SI, we found that $Ni(ClO_4)_2$ salts were removed by ethanol from silica surfaces based on the IR measurements (Figure S5), consistent with the computational predictions. When combined with the result in Figure 1b (black and green), we conclude that Ni^{2+} binds more strongly to the P(4VP-*co*-DVB) surface than glass.

Effect of coordinating polymer film on anchoring of 5CB

To evaluate the effects of the substrates (glass and P(4VP-*co*-DVB)) on the anchoring of 5CB, we performed DFT calculations with benzonitrile (PhCN, a surrogate molecule for 5CB, Scheme 1b). We calculated a G_{BE} of -0.70 eV for the interaction between the nitrile group of PhCN and the Ni^{2+} cation in the $Ni(ClO_4)_2$-hydroxylated silica complex ("salt+SiO_2" in Table 2 and Figure 2a left). The negative G_{BE} suggests that 5CB prefers to bind with the metal salt via the nitrile group, consistent with the past observation of a homeotropic orientation of 5CB on $Ni(ClO_4)_2$-decorated (≤ 1ML) glass surfaces.[52] The G_{BE} evaluated with the hydroxylated silica cluster in the model, however, is less negative (indicating weaker binding) than that calculated without the hydroxylated silica cluster (-1.04 eV; see past studies[52] and "salt only" in Table 2) due to electron donation from hydroxylated silica to Ni^{2+}. This suggests that binding of Ni^{2+} with a substrate can modulate the binding strength of Ni^{2+} with the LC. Based on this finding, we speculated that the stronger coordination interaction of Ni^{2+} with pyridine (-1.44 eV in Figure 1a) would further decrease the binding strength of the Ni^{2+} with PhCN, a prediction that was confirmed by DFT calculations (-0.57 eV for "salt+Pyr" in Table 2 and Figure 2a right). However, the G_{BE} of -0.57 eV of PhCN with Ni^{2+} in the $Ni(ClO_4)_2$-pyridine complex is still strong enough (< 0 eV) to lead us to predict that 5CB would assume a homeotropic orientation on the $Ni(ClO_4)_2$-decorated (≤ 1ML) P(4VP-*co*-DVB) surface based on previous benchmark studies.[52,55]

Table 2. Calculated G_{BE} of PhCN or DMMP or water to $Ni(ClO_4)_2$ (salt only), $Ni(ClO_4)_2$ coordinated with a hydroxylated silica cluster (salt+SiO_2) and $Ni(ClO_4)_2$ coordinated with a pyridine group (salt+Pyr), and calculated displacement free energy (G_{DE}) of PhCN by DMMP and by water. All values are in eV.

	G_{BE} of PhCN	G_{BE} of DMMP	G_{DE} by DMMP	G_{BE} of H_2O	G_{DE} by H_2O
salt	-1.04	-1.51	-0.47	-0.92	0.12
salt+SiO_2	-0.70	-1.11	-0.41	-0.82	-0.12
salt+Pyr	-0.57	-0.96	-0.39	-0.71	-0.14

Next, we performed experiments to characterize the anchoring of 5CB on the $Ni(ClO_4)_2$-decorated P(4VP-*co*-DVB) surface by confining 5CB between two metal salt-decorated surfaces under two crossed polarizers. We found 5CB to exhibit a dark optical appearance when confined by the P(4VP-*co*-DVB) surfaces decorated with 6.2±0.4 pmol/mm^2 $Ni(ClO_4)_2$ (Figure 2b, right column), consistent with a homeotropic orientation of 5CB and predictions of the above-described DFT calculations. To evaluate the prediction of a weaker binding of 5CB to $Ni(ClO_4)_2$ on the P(4VP-*co*-DVB) surfaces as compared to the glass surfaces, we performed experiments in which we decreased the surface density of Ni^{2+} binding sites on the P(4VP-*co*-DVB) surfaces (see SI for experimental methods). Specifically, we sought to determine the lowest surface density (LSD) of metal cation binding sites for which homeotropic anchoring of the LC was observed.[52] This experiment was motivated by our proposal that homeotropic anchoring can be induced by a small number (low LSD) of very strongly bound mesogens or, conversely, a large number (high LSD) of weakly bound mesogens on a surface. Inspection of the experimental results in Figure 2b reveals that the LSDs of $Ni(ClO_4)_2$ for glass and P(4VP-*co*-DVB) surfaces are 4.6±0.4 pmol/mm^2 and 6.2±0.4 pmol/mm^2, respectively. The measured ranking of the LSDs correlated inversely with the predicted G_{BE} values (glass: -0.70 eV and polymer: -0.57 eV). This result suggests a weaker binding of 5CB to the $Ni(ClO_4)_2$-decorated P(4VP-*co*-DVB) surface as compared to the $Ni(ClO_4)_2$-decorated glass surface, consistent with our DFT calculations.

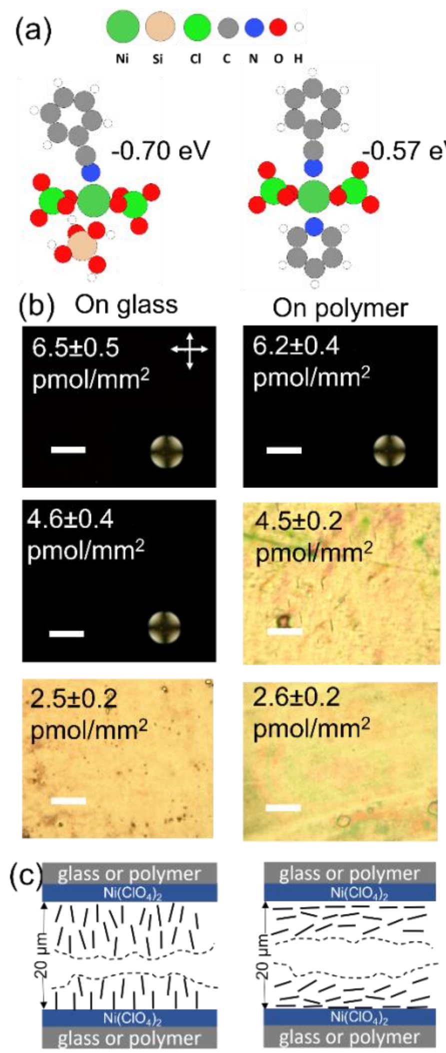

Figure 2. (a) Side view of the binding structure of PhCN with a $Ni(ClO_4)_2$ molecule coordinated with a hydroxylated silica cluster (left) or a pyridine molecule (right). (b) Cross-polarized images of 5CB films supported on $Ni(ClO_4)_2$-decorated glass and on polymer surfaces. The values of the surface density of Ni^{2+} are inserted in the images. The scale bars represent 100 μm. (c) Schematic illustration of the director profile of 5CB when it is sandwiched between two metal salt-decorated surfaces for homeotropic (left) and planar (right) LC anchoring.

Motivated by the results above, we then compared time-dependent changes in the ordering of 5CB supported on $Ni(ClO_4)_2$-decorated glass or P(4VP-*co*-DVB) surfaces (Figure 3). In these experiments, 5CB was hosted in transmission electron microscopy (TEM) grids to leave one side of the LC film exposed to a gaseous environment. When using the glass substrate to support the TEM grid, within 14 hours of equilibration of the LC in a dry N_2 environment, we observed the initial dark optical appearance of the LC (Figure 3a, 3b, left column) to disappear, indicating the loss of homeotropic anchoring of the LC (to tilted states) on the glass surface decorated with 8.5±0.5 pmol/mm^2 $Ni(ClO_4)_2$. A similar observation was reported previously for 5CB supported on carboxylic acid-terminated self-assembled monolayers decorated with 14.4 pmol/mm^2 $Al(ClO_4)_3$ (7 hours), an observation that was shown to be caused by dissolution of the salt into the LC.[58] In contrast to the glass substrate, we did not observe the optical appearance of 5CB supported on the P(4VP-*co*-DVB) surface decorated with 8.2±0.4 pmol/mm^2 $Ni(ClO_4)_2$ to change over 7 days of incubation (Figure 3d, 3e right column). These results support our prediction that cations can be displayed in a stable manner at the surfaces of coordinating polymers to orient LCs.

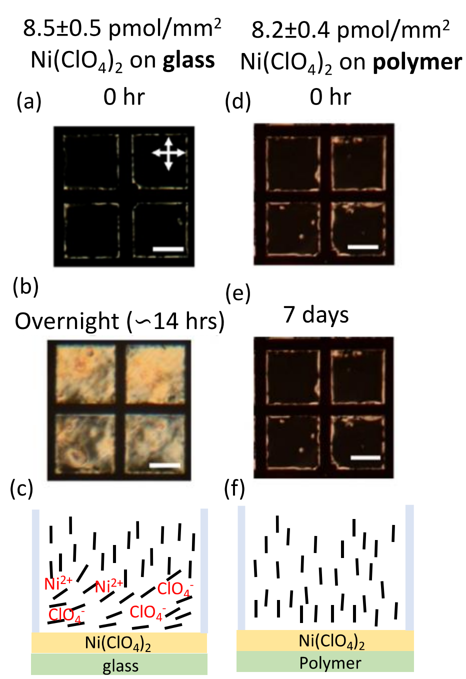

Figure 3. Cross-polarized images of 5CB films supported on (a),(b) $Ni(ClO_4)_2$-decorated glass or (d),(e) $Ni(ClO_4)_2$-decorated polymer surfaces stored under dry N_2 environment. (c) Schematic illustration of dissolution of $Ni(ClO_4)_2$ from glass to bulk 5CB which leads to a planar anchoring of 5CB. (f) Schematic illustration of homeotropic anchoring of 5CB on $Ni(ClO_4)_2$ on polymer under dry nitrogen. The scale bars represent 200 μm.

Effect of coordinating polymer film on adsorbate-driven change in anchoring of 5CB

To predict whether the LC would respond to DMMP, we calculated the change in free energy accompanying displacement (G_{DE}) of 5CB by DMMP from a complex of $Ni(ClO_4)_2$ with hydroxylated silica or pyridine. Our calculations predict G_{DE} of 5CB by DMMP to be -0.41 eV or -0.39 eV for the complex with hydroxylated silica or pyridine, respectively, indicating that displacement by DMMP is a thermodynamically favored process in both environments (Table 2 and Figure 4a). In our past work, we observed that a threshold value of G_{DE} of -0.4 ~ -0.5 eV correlated with the onset of experimentally observed displacement processes.[52,53,55] The existence of the threshold, which likely reflects kinetic effects but remains to be fully understood, makes prediction of the outcome of experiments performed on silica and pyridine surfaces uncertain based on the above-calculated values of G_{DE}.

To address this uncertainty, we performed experiments to characterize the response of 5CB on the $Ni(ClO_4)_2$-decorated glass or P(4VP-*co*-DVB) surfaces by quantifying the optical appearance of 5CB to exposure to 10 ppm DMMP. As shown in Figure 4b (open black squares), 5CB supported on the glass surface decorated with 8.5±0.5 pmol/mm^2 $Ni(ClO_4)_2$ (~1ML coverage) exhibited no measurable orientational response upon exposure to 10 ppm DMMP for 1 hour. A similar observation was reported previously when using $Ni(ClO_4)_2$ with a surface density of ~100 pmol/mm^2 (multiple layers of salts).[52] When using P(4VP-*co*-DVB) as the substrate for 8.2±0.4 pmol/mm^2 $Ni(ClO_4)_2$ (solid squares in Figure 4b), however, we observed a dynamic orientational transition of 5CB to start within 10 mins of exposure to DMMP. The optical response of the 5CB film concluded 25 mins after the onset of exposure (set the normalized light intensity as 1; bright optical appearance shown in the inset of Figure 4b). The change in optical appearance of the LC film was reversed upon subsequent exposure to dry N_2 (red squares), and further reversed over several subsequent cycles of DMMP and N_2 exposure. The observation of a 5CB response to DMMP on the coordinating polymer substrate but an absence of response on the glass substrate is interesting in light of the similar G_{DE} values (-0.39 eV and -0.41 eV, respectively) predicted by our DFT calculations. This result raises the possibility that the distinct response of the LC on glass and the coordinating polymer surface reflects the kinetics, rather than the thermochemistry, of the displacement reaction at the surface.

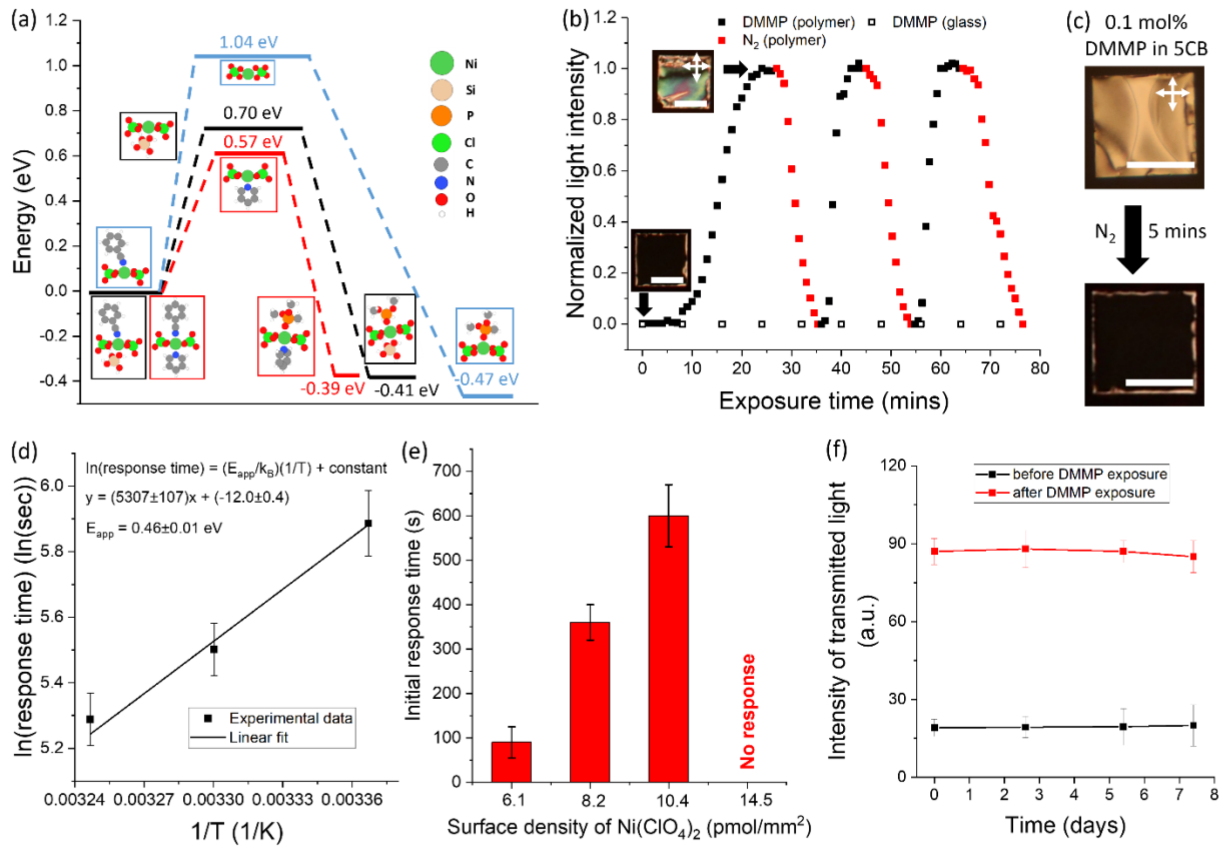

Figure 4. (a) Calculated potential energy diagram of the displacement of PhCN by DMMP on $Ni(ClO_4)_2$ only (blue) or on $Ni(ClO_4)_2$ coordinated with a hydroxylated silica cluster (black) or a pyridine molecule (red). The energies of bound PhCN states are set to 0 eV. The boxed insets are the minimum-energy binding structures (side view) associated with the states (horizontal lines) near them. The boxes are color-coded to correspond to the relevant potential energy diagram. (b) Normalized intensity of polarized light transmitted through 5CB supported on the P(4VP-*co*-DVB) surface decorated with 8.2±0.4 pmol/mm^2 $Ni(ClO_4)_2$ during cycles of exposure to 10 ppm DMMP (solid black squares) and N_2 (solid red squares). The insets are the optical micrographs (crossed polarizers) of 5CB at t=0 min and t=25 min. The open black squares indicate the response of 5CB supported on the glass surface decorated with 8.5±0.5 pmol/mm^2 $Ni(ClO_4)_2$ during exposure to 10 ppm DMMP for over 1 hour. (c) Cross-polarized images of DMMP-5CB (C_{DMMP}=0.1 mol%) supported on the glass surface decorated with 8.5±0.5 pmol/mm^2 $Ni(ClO_4)_2$

before and after exposure to N_2 for 5 mins. (d) Initial response times (the interval of time between the introduction of DMMP and measurement of 10% of the normalized light intensity of the full response) of 5CB supported on P(4VP-*co*-DVB) surfaces decorated with 8.2±0.4 pmol/mm^2 $Ni(ClO_4)_2$ to 10 ppm DMMP at different temperatures (24°C, 30°C and 34°C) (e) Initial response time of 5CB supported on P(4VP-*co*-DVB) surfaces decorated with various surface densities of $Ni(ClO_4)_2$ following exposure to 10 ppm DMMP. (f) Effects of storage on the orientations of 5CB supported on P(4VP-*co*-DVB) surfaces decorated with 8.2±0.4 pmol/mm^2 $Ni(ClO_4)_2$ before (black) and after (red) exposure to 10 ppm DMMP. The samples were stored in dry N_2 and at room temperature. The scale bars represent 200 μm.

To address the possible role of kinetics, we considered a simple model for an intermediate state of the system during the process of displacement of 5CB by DMMP (Figure 4a). In this model, the bound PhCN first desorbs from Ni^{2+} to generate a free Ni^{2+} binding site, and then DMMP binds to the Ni^{2+}. The energy to break the PhCN-Ni^{2+} coordination interaction thus provides an estimate for the kinetic barrier for displacement, which is estimated as the negative of G_{BE} of PhCN. Figure 4a shows that displacement of PhCN by DMMP when using pyridine (red) is characterized by an estimated kinetic barrier (0.57 eV) that is 0.13 eV lower than when using hydroxylated silica (black) due to the weaker G_{BE} of PhCN to Ni^{2+} coordinated with pyridine (as compared to with hydroxylated silica in Table 2 and Figure 2a). We note that a change in the energy of 0.06 eV corresponds to a 1 order of magnitude change in reaction rate at room temperature; thus, the considerations described above predict a response to DMMP on the glass substrate that is slower by ~2 orders of magnitude as compared to the P(4VP-*co*-DVB) film. This result is consistent with the experimental observation of the absence of any response within 70 mins on the glass substrate and an initial response on the P(4VP-*co*-DVB) substrate within 10 mins of onset of exposure to DMMP.

To explore further if the response of 5CB to DMMP is kinetically hindered on the $Ni(ClO_4)_2$-decorated glass substrate, we mixed liquid DMMP with 5CB and then characterized the anchoring of the DMMP-5CB mixture on a $Ni(ClO_4)_2$-decorated glass substrate. In this experiment, we predicted, based on our DFT calculations, that some Ni^{2+} binding sites would be occupied by DMMP molecules when contacted with the DMMP-5CB mixture. Inspection of Figure 4c reveals that the DMMP-5CB mixture (C_{DMMP}=0.1 mol%) adopted a planar orientation on the glass surface decorated with 8.5±0.5 pmol/mm^2 $Ni(ClO_4)_2$, consistent with this prediction. Additionally, a transition from planar to homeotropic anchoring of the DMMP-5CB mixture occurred within 5 mins of exposure of the sample to N_2 (Figure 4c). This result further suggests that DMMP molecules bound at the $Ni(ClO_4)_2$ interface prior to N_2 exposure caused the planar orientation of the LC. Overall, these experiments support the idea that DMMP binds more strongly than 5CB to the $Ni(ClO_4)_2$-decorated glass substrate, as suggested by our calculations (Table 2), and that the lack of response of 5CB on the $Ni(ClO_4)_2$-decorated glass substrate to DMMP vapor (Figure 4b, open black squares) is likely due to the kinetics of the displacement reaction.

The results described above support our proposal that the response of 5CB to DMMP is governed by the kinetics of the displacement reaction. This led us to predict that the LC response to DMMP would be faster at a higher temperature when 5CB was supported on the $Ni(ClO_4)_2$-decorated P(4VP-*co*-DVB) surface. Motivated by this prediction, we evaluated the LC response dynamics as the temperature was increased from 24^{o}C to 34^{o}C (the nematic-to-isotropic transition temperature of 5CB is 35^{o}C[93]). Inspection of Figure 4d reveals that 5CB exhibited a faster response to DMMP at the higher temperature. We also determined the natural log of the initial response time to be proportional to the inverse of temperature, consistent with an Arrhenius-type expression (the equation in Figure 4d). By using the slope of the linear fit to the experimental data, we determined an apparent activation energy of 0.46±0.1 eV for the displacement of 5CB by DMMP on P(4VP-*co*-DVB) surfaces decorated with 8.2±0.4 pmol/mm^2 $Ni(ClO_4)_2$. This experimentally determined apparent activation energy is in good agreement with the one obtained from our DFT calculations (0.57 eV in Figure 4a). We end by noting that the change of the diffusion coefficient of DMMP in air or the LC upon heating from 24^{o}C to 34^{o}C is small,[94] suggesting that changes in response times in Figure 4d are not likely dominated by mass transport.[50] Overall, these results provide support for our proposal that the displacement of 5CB by DMMP is a kinetically controlled process.

In the above-described results, we used a surface density of ~8 pmol/mm^2 of $Ni(ClO_4)_2$. We also performed measurements of the response of 5CB to DMMP supported on P(4VP-*co*-DVB) surfaces decorated with lower surface densities of $Ni(ClO_4)_2$. Inspection of Figure 4e reveals that 5CB exhibited a faster orientational transition on the P(4VP-*co*-DVB) surface decorated with 6.1±0.4 pmol/mm^2 $Ni(ClO_4)_2$ than 8.2±0.4 pmol/mm^2 $Ni(ClO_4)_2$. We hypothesized that these dynamics arise because DMMP has to displace more 5CB molecules bound to Ni^{2+} when using the higher density of Ni^{2+} ions on the surface. To test this hypothesis, we increased the surface density of Ni^{2+} to 10.4±0.3 pmol/mm^2 and observed 5CB to exhibit a slower response to DMMP than when it was supported on 8.2±0.4 pmol/mm^2 $Ni(ClO_4)_2$ (Figure 4e). When we further increased the surface density to 14.5±0.5 pmol/mm^2, however, we did not observe a response of 5CB to DMMP in 1 hour. We note that the surface density of 14.5±0.5 pmol/mm^2 corresponds to ~1.8 ML metal salt coverage (8.4 pmol/mm^2 for 1 ML $Ni(ClO_4)_2$). Under these conditions, it is possible that the top layer of Ni^{2+} ions bound to 5CB are not coordinating with the pyridine groups of the polymer substrate. Accordingly, the kinetic barrier for the displacement of 5CB by DMMP is large (1.04 eV, Figure 4a blue), above what is kinetically feasible at room temperature.

We next determined if the anchoring transition induced by DMMP changed with the age of the metal salt-decorated polymer surfaces. After the 5CB samples were stored for a desired length of time (room temperatures; dry conditions), we characterized the LC before and after exposure to DMMP. As shown in Figure 4f and reported above, immediately after preparation of samples and prior to exposure to DMMP, 5CB exhibited homeotropic anchoring on the P(4VP-*co*-DVB) surface decorated with 8.2±0.4 pmol/mm^2 $Ni(ClO_4)_2$. The corresponding intensity of light transmitted through samples was low (19±3 a.u.). The anchoring transition of 5CB induced by exposure to DMMP resulted in an increase in the intensity of light transmitted through samples to 87±5 a.u. (the changes in the light intensity were reversed upon subsequent exposure to N_2). Following storage of the LCs for over 2, 5, and 7 days, we observed the initial homeotropic anchoring of the LCs (19±5 a.u.) to be stable and the response to DMMP to occur without significant change in dynamics or endpoint (67±6 a.u.). These results demonstrate that metal-coordinating polymer surfaces represent a promising class of substrates for the design of stable and long-lived chemoresponsive LCs (recall that LCs on glass substrates lost their homeotropic anchoring in 14 hrs).

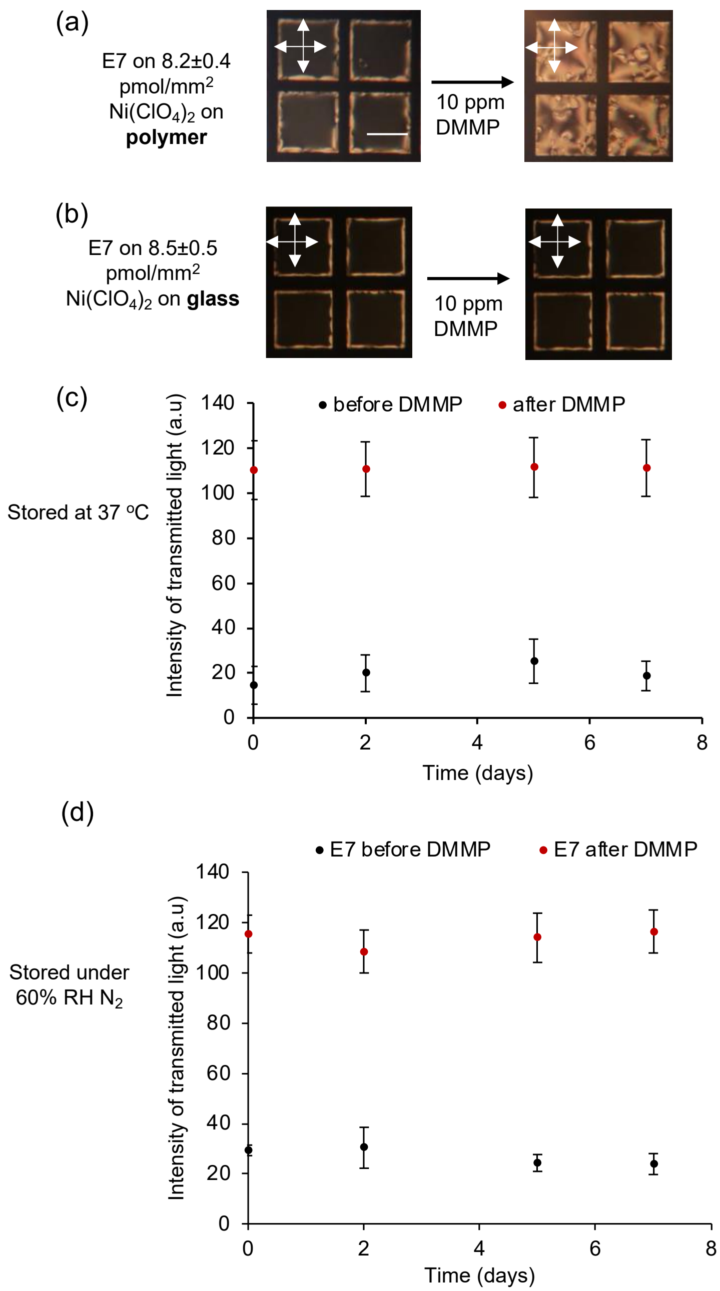

Figure 5: Cross-polarized images of E7 films supported on (a) 8.2±0.4 pmol/mm^2 $Ni(ClO_4)_2$-decorated P(4VP-*co*-DVB) or (b) 8.5±0.5 pmol/mm^2 $Ni(ClO_4)_2$ glass surfaces and their response to 10 ppm DMMP. (c) Quantification of optical appearance of E7 on 8.2±0.4 pmol/mm^2 $Ni(ClO_4)_2$ on P(4VP-*co*-DVB) before (black) and after (red) exposure to 10 ppm DMMP when stored at 37 ^{o}C. (d) Quantification of optical appearance of E7 on 8.2±0.4 pmol/mm^2 $Ni(ClO_4)_2$

on P(4VP-*co*-DVB) before (black) and after (red) exposure to 10 ppm DMMP when stored under 60% RH N_2. Scale bar: 200 μm.

Chemoresponse of LC with a wide nematic temperature range

5CB is a model LC that is comprised of a single component. The single component nature of the LC is helpful for fundamental studies, but the limited temperature range over which 5CB exhibits a nematic phase (22.5 °C-35.3 °C)[95] means that it is not a technological LC. In contrast, the LC called E7, which comprises four components (see Figure S13), possesses a nematic phase that is stable from -10 °C to 57.8 °C.[96] To determine if the use of metal coordinating polymer films can also improve the design of chemoresponsive systems based on technological LCs, we next evaluated the use of coordinating polymer films formed from P(4VP-*co*-DVB) in combination with E7. We began an evaluation of E7 by determining if it assumes a homeotropic orientation and responds to 10 ppm DMMP when supported on 8.2±0.4 pmol/mm² $Ni(ClO_4)_2$ on P(4VP-*co*-DVB) surfaces as well as on 8.5±0.5 pmol/mm² $Ni(ClO_4)_2$ on glass. Inspection of Figure 5a and Figure 5b reveals that E7 does exhibit homeotropic anchoring on these surfaces and, similar to 5CB, exhibits a reversible response to 10 ppm DMMP when using $Ni(ClO_4)_2$ on P(4VP-*co*-DVB) but not $Ni(ClO_4)_2$ on glass (Figure 5b).

Next, we evaluated the stability of E7 anchoring on 8.2±0.4 pmol/mm² $Ni(ClO_4)_2$ on P(4VP-*co*-DVB) and its response to 10 ppm DMMP when stored for a period of 2, 5 or 7 days at an elevated temperature (37 °C) or in the presence of 60% RH. Inspection of Figure 5c (black data points) reveals that the light intensity transmitted through E7 on $Ni(ClO_4)_2$ on P(4VP-*co*-DVB) before exposure to 10 ppm DMMP was stable with storage at 37 °C and consistent with homeotropic anchoring. Furthermore, the response of E7 to 10 ppm DMMP also did not change over a period of 7 days of storage at 37 ºC (after the response, the intensity of transmitted light was consistently 110±13 a.u). Similar levels of performance (stability to storage and consistency of response to DMMP) were observed when the E7 samples supported on 8.2±0.4 pmol/mm^2 $Ni(ClO_4)_2$ on P(4VP-*co*-DVB) were stored at 60% RH N_2 and then exposed to DMMP (Figure 5d).

We further note that E7 is stable to exposure to 60% RH N_2 on a 8.2±0.4 pmol/mm^2 $Ni(ClO_4)_2$ on P(4VP-co-DVB) substrates whereas 5CB is not stable under these conditions (described in SI Figure S11), despite both LCs containing nitrile-terminated mesogens. DFT calculations conducted in this study used the PhCN molecule as a surrogate for 5CB and predicted that PhCN is displaced by water on $Ni(ClO_4)_2$ coordinated with pyridine (consistent with experimental observations with 5CB). In contrast, the DFT predictions based on PhCN do not agree with experiments performed with E7. Because E7 is a mixture, we do not know which molecular components of E7 dominate the interfacial behavior of the LC. Our results suggest that PhCN is not an appropriate surrogate for predicting the behavior of E7. Overall, however, our experimental observations with E7 suggest that the benefits of using metal ion coordinating polymer films for the design of chemoresponsive systems extend to technological LCs comprised of mixtures of mesogens.

CONCLUSIONS

This work reports the design of chemoresponsive LCs using metal-coordinating polymer films and explores effects of the coordinating interfacial environment on the ordering and time-dependent properties of LCs. The design, which was guided by electronic structure calculations, uses pyridine groups in P(4VP-*co*-DVB) thin films deposited by iCVD to coordinate with metal cations. Computational predictions that the metal ion-pyridine coordination interaction would weaken the binding of 5CB were validated by experiments in which we compared anchoring of 5CB supported on glass or P(4VP-*co*-DVB) substrates. Additionally, we discovered that DMMP triggers an orientational transition of 5CB supported on the $Ni(ClO_4)_2$-decorated polymer substrates, but not on the glass substrates decorated with a similar surface density of $Ni(ClO_4)_2$. We interpreted the distinct responses to reflect the kinetics of the displacement reaction, an interpretation that is supported by temperature-dependent measurements of the dynamic response of LCs to DMMP. Importantly, by presenting metal cation binding sites from P(4VP-*co*-DVB) substrates, we measured substantial improvements in the stability of chemoresponsive LCs to long-term storage, with a technological LC exhibiting stable orientations and reproducible responses to DMMP when stored at elevated temperatures and humidity conditions. Overall, these results demonstrate that metal-coordinating polymer films are a promising class of substrates for designing chemoresponsive LC-based systems. Our results also generate a range of questions: (i) do metal ion-pyridine coordination interactions induce changes in the surface morphology of polymer films (e.g., roughness and microscale or macroscale structures[97–99]) and further change the distribution of metal ions on the surface?; (ii) can we use polymers with functional groups other than pyridine (e.g., nitrile[100] or amine[101]) to coordinate with metal ions to modulate LC/analyte-metal ion interactions and thereby explore further kinetic effects on the response of LCs to chemical environment (or other chemical species)? Additionally, our study hints that other classes of metal-ion-containing polymers[102] or metal-organic frameworks[103] may be potentially promising substrates for designing chemoresponsive LCs.

ASSOCIATED CONTENT

Supporting Information

Additional computational details, additional experimental details, additional spectroscopic characterization and optical images (PDF)

AUTHOR INFORMATION

Corresponding Author

*ryang@cornell.edu (Rong Yang)

*emavrikakis@wisc.edu (Manos Mavrikakis)

*nla34@cornell.edu (Nicholas L. Abbott)

Author Contributions

N.B., M.M., and N.L.A. conceived and coordinated the study. N.B. and A.T. performed the experiments and analyzed the results. T.F. and R.Y. synthesized the polymer thin films. M.M. supervised and T.S. and T.J.W. performed the electronic structure calculations. N.B., N.L.A., R.J.T., M.M., and R.Y. wrote the manuscript with input from all authors.

Notes

N.L.A. declares a financial interest in Platypus Technologies LLC, a for-profit company that has developed LC-based analytic technologies.

ACKNOWLEDGMENT

This work was supported by the National Science Foundation (DMREF grant: DMR-1921696, DMR-1921722, and DMR-1921668; and Future Manufacturing Research Grant: CMMI-

2229092). Part of the computational work was carried out through external computational facilities at: the National Energy Research Scientific Computing Center (NERSC) supported by the U.S. DOE, Office of Science under Contract No. DE-AC02-05CH11231, using NERSC award BES-ERCAP0019973. This material is based upon work supported by the National Science Foundation Graduate Research Fellowship Program under grant DGE-1650441 to T.F. Any opinions, findings, conclusions, or recommendations expressed in this material are those of the author(s) and do not necessarily reflect the views of the National Science Foundation.

REFERENCES

(1) H.-J. Schneider. *Chemoresponsive Materials*; RSC Smart Materials: London, 2015.

(2) Zarzar, L. D.; Aizenberg, J. Stimuli-Responsive Chemomechanical Actuation: A Hybrid Materials Approach. *Acc Chem Res* **2014**, *47* (2), 530–539. https://doi.org/10.1021/ar4001923.

(3) Shah, R. R.; Abbott, N. L. Principles for Measurement of Chemical Exposure Based on Recognition-Driven Anchoring Transitions in Liquid Crystals. *Science (1979)* **2001**, *293* (5533), 1296–1299. https://doi.org/10.1126/science.1062293.

(4) Beebe, D. J.; Moore, J. S.; Bauer, J. M.; Yu, Q.; Liu, R. H.; Devadoss, C.; Jo, B. H. Functional Hydrogel Structures for Autonomous Flow Control inside Microfluidic Channels. *Nature* **2000**, *404* (6778), 588–590. https://doi.org/10.1038/35007047.

(5) Caldorera-Moore, M. E.; Liechty, W. B.; Peppas, N. A. Responsive Theranostic Systems: Integration of Diagnostic Imaging Agents and Responsive Controlled Release Drug Delivery Carriers. *Acc Chem Res* **2011**, *44* (10), 1061–1070. https://doi.org/10.1021/ar2001777.

(6) Prévôt, M. E.; Nemati, A.; Cull, T. R.; Hegmann, E.; Hegmann, T. A Zero-Power Optical, Ppt- to Ppm-Level Toxic Gas and Vapor Sensor with Image, Text, and Analytical Capabilities. *Adv Mater Technol* **2020**, *5* (5), 1–11. https://doi.org/10.1002/admt.202000058.

(7) Schwartz, M.; Lagerwall, J. P. F. Embedding Intelligence in Materials for Responsive Built Environment: A Topical Review on Liquid Crystal Elastomer Actuators and Sensors. *Build Environ* **2022**, *226* (October), 109714. https://doi.org/10.1016/j.buildenv.2022.109714.

(8) Rouhbakhsh, Z.; Huang, J. W.; Ho, T. Y.; Chen, C. H. Liquid Crystal-Based Chemical Sensors and Biosensors: From Sensing Mechanisms to the Variety of Analytical Targets. *TrAC - Trends in Analytical Chemistry* **2022**, *157*, 116820. https://doi.org/10.1016/j.trac.2022.116820.

(9) Lagerwall, J. Liquid Crystal Elastomer Actuators and Sensors: Glimpses of the Past, the Present and Perhaps the Future. *Programmable Materials* **2023**, *1*. https://doi.org/10.1017/pma.2023.8.

(10) Perera, K.; Dassanayake, T. M.; Jeewanthi, M.; Haputhanthrige, N. P.; Huang, S. D.; Kooijman, E.; Mann, E.; Jákli, A. Liquid Crystal-Based Detection of Antigens with ELISA Sensitivity. *Adv Mater Interfaces* **2022**, *9* (25), 25–29. https://doi.org/10.1002/admi.202200891.

(11) Guan, Y.; Agra-Kooijman, D. M.; Fu, S.; Jákli, A.; West, J. L. Responsive Liquid-Crystal-Clad Fibers for Advanced Textiles and Wearable Sensors. *Advanced Materials* **2019**, *31* (29), 1–5. https://doi.org/10.1002/adma.201902168.

(12) Wang, J.; Jákli, A.; West, J. L. Liquid Crystal/Polymer Fiber Mats as Sensitive Chemical Sensors. *J Mol Liq* **2018**, *267*, 490–495. https://doi.org/10.1016/j.molliq.2018.01.051.

(13) Kurt, E.; Bukusoglu, E. Liquid Crystal Microcapillary-Based Sensors for Affordable Analytical Applications. *Soft Matter* **2022**, *18* (20), 4009–4016. https://doi.org/10.1039/d2sm00131d.

(14) Kim, I.; Kim, W. S.; Kim, K.; Ansari, M. A.; Mehmood, M. Q.; Badloe, T.; Kim, Y.; Gwak, J.; Lee, H.; Kim, Y. K.; Rho, J. Holographic Metasurface Gas Sensors for Instantaneous Visual Alarms. *Sci Adv* **2021**, *7* (15). https://doi.org/10.1126/SCIADV.ABE9943.

(15) Schelski, K.; Reyes, C. G.; Pschyklenk, L.; Kaul, P. M.; Lagerwall, J. P. F. Quantitative Volatile Organic Compound Sensing with Liquid Crystal Core Fibers. *Cell Rep Phys Sci* **2021**, *2* (12), 100661. https://doi.org/10.1016/j.xcrp.2021.100661.

(16) Xu, Y.; Rather, A. M.; Song, S.; Fang, J. C.; Dupont, R. L.; Kara, U. I.; Chang, Y.; Paulson, J. A.; Qin, R.; Bao, X.; Wang, X. Ultrasensitive and Selective Detection of SARS-CoV-2 Using Thermotropic Liquid Crystals and Image-Based Machine Learning. *Cell Rep Phys Sci* **2020**, *1* (12), 100276. https://doi.org/10.1016/j.xcrp.2020.100276.

(17) Popov, P.; Mann, E. K.; Jákli, A. Thermotropic Liquid Crystal Films for Biosensors and Beyond. *J Mater Chem B* **2017**, *5* (26), 5061–5078. https://doi.org/10.1039/c7tb00809k.

(18) Yokoyama, H. Surface Anchoring of Nematic Liquid Crystals. *Molecular Crystals and Liquid Crystals Incorporating Nonlinear Optics* **1988**, *165*, 265–361. https://doi.org/10.1080/00268948808082204.

(19) Jerome, B. Surface Effects and Anchoring in Liquid Crystals. *Reports on Progress in Physics* **1991**, *54*, 391–451. https://doi.org/10.1088/0034-4885/54/3/002.

(20) Kocaman, C.; Batir, O.; Bukusoglu, E. Optically Responsive Dry Cholesteric Liquid Crystal Marbles. *J Colloid Interface Sci* **2024**, *671* (April), 374–384. https://doi.org/10.1016/j.jcis.2024.05.194.

(21) Honaker, L. W.; Chen, C.; Dautzenberg, F. M. H.; Brugman, S.; Deshpande, S. Designing Biological Microsensors with Chiral Nematic Liquid Crystal Droplets. *ACS Appl Mater Interfaces* **2022**, *14* (33), 37316–37329. https://doi.org/10.1021/acsami.2c06923.

(22) Sezer, S.; Bukusoglu, E. Nanoparticle-Assisted Liquid Crystal Droplet Sensors Enable Analysis of Low-Concentration Species in Aqueous Medium. *Langmuir* **2024**, *40* (6), 3154–3167. https://doi.org/10.1021/acs.langmuir.3c03598.

(23) Ortiz, B. J.; Boursier, M. E.; Barrett, K. L.; Manson, D. E.; Amador-Noguez, D.; Abbott, N. L.; Blackwell, H. E.; Lynn, D. M. Liquid Crystal Emulsions That Intercept and Report on Bacterial Quorum Sensing. *ACS Appl Mater Interfaces* **2020**, *12* (26), 29056–29065. https://doi.org/10.1021/acsami.0c05792.

(24) Xie, R.; Li, N.; Li, Z.; Chen, J.; Li, K.; He, Q.; Liu, L.; Zhang, S. Liquid Crystal Droplet-Based Biosensors: Promising for Point-of-Care Testing. *Biosensors (Basel)* **2022**, *12* (9). https://doi.org/10.3390/bios12090758.

(25) Manna, U.; Zavala, Y. M.; Abbott, N. L.; Lynn, D. M. Structured Liquid Droplets as Chemical Sensors That Function Inside Living Cells. *ACS Appl Mater Interfaces* **2021**, *13* (36), 42502–42512. https://doi.org/10.1021/acsami.1c12667.

(26) Ramou, E.; Palma, S. I. C. J.; Roque, A. C. A. Nanoscale Events on Cyanobiphenyl-Based Self-Assembled Droplets Triggered by Gas Analytes. *ACS Appl Mater Interfaces* **2022**, *14* (4), 6261–6273. https://doi.org/10.1021/acsami.1c24721.

(27) Concellón, A.; Fong, D.; Swager, T. M. Complex Liquid Crystal Emulsions for Biosensing. *J Am Chem Soc* **2021**, *143* (24), 9177–9182. https://doi.org/10.1021/jacs.1c04115.

(28) White, T. J.; McConney, M. E.; Bunning, T. J. Dynamic Color in Stimuli-Responsive Cholesteric Liquid Crystals. *J Mater Chem* **2010**, *20* (44), 9832. https://doi.org/10.1039/c0jm00843e.

(29) Sutarlie, L.; Qin, H.; Yang, K.-L. Polymer Stabilized Cholesteric Liquid Crystal Arrays for Detecting Vaporous Amines. *Analyst* **2010**, *135* (7), 1691. https://doi.org/10.1039/b926674g.

(30) Chang, C.-K.; Kuo, H.-L.; Tang, K.-T.; Chiu, S.-W. Optical Detection of Organic Vapors Using Cholesteric Liquid Crystals. *Appl Phys Lett* **2011**, *99* (7), 073504. https://doi.org/10.1063/1.3627162.

(31) Saha, A.; Tanaka, Y.; Han, Y.; Bastiaansen, C. M. W.; Broer, D. J.; Sijbesma, R. P. Irreversible Visual Sensing of Humidity Using a Cholesteric Liquid Crystal. *Chemical Communications* **2012**, *48* (38), 4579. https://doi.org/10.1039/c2cc16934g.

(32) Su, X.; Voskian, S.; Hughes, R. P.; Aprahamian, I. Manipulating Liquid-Crystal Properties Using a PH Activated Hydrazone Switch. *Angewandte Chemie International Edition* **2013**, *52* (41), 10734–10739. https://doi.org/10.1002/anie.201305514.

(33) Cachelin, P.; Green, J. P.; Peijs, T.; Heeney, M.; Bastiaansen, C. W. M. Optical Acetone Vapor Sensors Based on Chiral Nematic Liquid Crystals and Reactive Chiral Dopants. *Adv Opt Mater* **2016**, *4*, 592–596. https://doi.org/10.1002/adom.201500549.

(34) Yang, Y.; Kim, Y.-K.; Wang, X.; Tsuei, M.; Abbott, N. L. Structural and Optical Response of Polymer-Stabilized Blue Phase Liquid Crystal Films to Volatile Organic Compounds. *ACS Appl Mater Interfaces* **2020**, *12* (37), 42099–42108. https://doi.org/10.1021/acsami.0c11138.

(35) Pschyklenk, L.; Wagner, T.; Lorenz, A.; Kaul, P. Optical Gas Sensing with Encapsulated Chiral-Nematic Liquid Crystals. *ACS Appl Polym Mater* **2020**, *2* (5), 1925–1932. https://doi.org/10.1021/acsapm.0c00142.

(36) Schelski, K.; Reyes, C. G.; Pschyklenk, L.; Kaul, P.-M.; Lagerwall, J. P. F. Quantitative Volatile Organic Compound Sensing with Liquid Crystal Core Fibers. *Cell Rep Phys Sci* **2021**, 100661. https://doi.org/10.1016/j.xcrp.2021.100661.

(37) Szilvási, T.; Bao, N.; Nayani, K.; Yu, H.; Rai, P.; Twieg, R. J.; Mavrikakis, M.; Abbott, N. L. Redox-Triggered Orientational Responses of Liquid Crystals to Chlorine Gas. *Angewandte Chemie International Edition* **2018**, *57* (31), 9665–9669. https://doi.org/10.1002/anie.201803194.

(38) Nayani, K.; Rai, P.; Bao, N.; Yu, H.; Mavrikakis, M.; Twieg, R. J.; Abbott, N. L. Liquid Crystals with Interfacial Ordering That Enhances Responsiveness to Chemical Targets. *Advanced Materials* **2018**, *30* (27), 1706707. https://doi.org/10.1002/adma.201706707.

(39) Brake, J. M.; Daschner, M. K.; Luk, Y. Y.; Abbott, N. L. Biomolecular Interactions at Phospholipid-Decorated Surfaces of Liquid Crystals. *Science (1979)* **2003**, *302*, 2094–2097. https://doi.org/10.1126/science.1091749.

(40) Bi, X.; Hartono, D.; Yang, K. L. Real-Time Liquid Crystal PH Sensor for Monitoring Enzymatic Activities of Penicillinase. *Adv Funct Mater* **2009**, *19* (23), 3760–3765. https://doi.org/10.1002/adfm.200900823.

(41) Popov, P.; Mann, E. K.; Jákli, A. Accurate Optical Detection of Amphiphiles at Liquid-Crystal-Water Interfaces. *Phys Rev Appl* **2014**, *1* (3), 1–9. https://doi.org/10.1103/PhysRevApplied.1.034003.

(42) Sen, A.; Kupcho, K. A.; Grinwald, B. A.; Vantreeck, H. J.; Acharya, B. R. Liquid Crystal-Based Sensors for Selective and Quantitative Detection of Nitrogen Dioxide. *Sens Actuators B Chem* **2013**, *178*, 222–227. https://doi.org/10.1016/j.snb.2012.12.036.

(43) Bao, N.; Jiang, S.; Smith, A.; Schauer, J. J.; Mavrikakis, M.; Van Lehn, R. C.; Zavala, V. M.; Abbott, N. L. Sensing Gas Mixtures by Analyzing the Spatiotemporal Optical Responses of Liquid Crystals Using 3D Convolutional Neural Networks. *ACS Sens* **2022**, *7* (9), 2545–2555. https://doi.org/10.1021/acssensors.2c00362.

(44) Yu, H.; Gold, J. I.; Wolter, T. J.; Bao, N.; Smith, E.; Zhang, H. A.; Twieg, R. J.; Mavrikakis, M.; Abbott, N. L. Actuating Liquid Crystals Rapidly and Reversibly by Using Chemical Catalysis. *Advanced Materials* **2024**, *2309605*, 1–13. https://doi.org/10.1002/adma.202309605.

(45) Woltman, S. J.; Jay, G. D.; Crawford, G. P. Liquid-Crystal Materials Find a New Order in Biomedical Applications. *Nat Mater* **2007**, *6*, 929–938. https://doi.org/10.1038/nmat2010.

(46) Esteves, C.; Ramou, E.; Porteira, A. R. P.; Moura Barbosa, A. J.; Roque, A. C. A. Seeing the Unseen: The Role of Liquid Crystals in Gas-Sensing Technologies. *Adv Opt Mater* **2020**, *8* (11), 1902117. https://doi.org/10.1002/adom.201902117.

(47) Nayani, K.; Rai, P.; Bao, N.; Yu, H.; Mavrikakis, M.; Twieg, R. J.; Abbott, N. L. Liquid Crystals with Interfacial Ordering That Enhances Responsiveness to Chemical Targets. *Advanced Materials* **2018**, *30* (27), 1–7. https://doi.org/10.1002/adma.201706707.

(48) Yang, K. L.; Cadwell, K.; Abbott, N. L. Mechanistic Study of the Anchoring Behavior of Liquid Crystals Supported on Metal Salts and Their Orientational Responses to Dimethyl

Methylphosphonate. *Journal of Physical Chemistry B* **2004**, *108* (52), 20180–20186. https://doi.org/10.1021/jp0470391.

(49) Hunter, J. T.; Pal, S. K.; Abbott, N. L. Adsorbate-Induced Ordering Transitions of Nematic Liquid Crystals on Surfaces Decorated with Aluminum Perchlorate Salts. *ACS Appl Mater Interfaces* **2010**, *2* (7), 1857–1865. https://doi.org/10.1021/am100165a.

(50) Hunter, J. T.; Abbott, N. L. Dynamics of the Chemo-Optical Response of Supported Films of Nematic Liquid Crystals. *Sens Actuators B Chem* **2013**, *183*, 71–80. https://doi.org/10.1016/j.snb.2013.03.094.

(51) Hunter, J. T.; Pal, S. K.; Abbott, N. L. Adsorbate-Induced Ordering Transitions of Nematic Liquid Crystals on Surfaces Decorated with Aluminum Perchlorate Salts. *ACS Appl Mater Interfaces* **2010**, *2* (7), 1857–1865. https://doi.org/10.1021/am100165a.

(52) Szilvási, T.; Bao, N.; Yu, H.; Twieg, R. J.; Mavrikakis, M.; Abbott, N. L. The Role of Anions in Adsorbate-Induced Anchoring Transitions of Liquid Crystals on Surfaces with Discrete Cation Binding Sites. *Soft Matter* **2018**, *14* (5), 797–805. https://doi.org/10.1039/c7sm01981e.

(53) Yu, H.; Szilvási, T.; Rai, P.; Twieg, R. J.; Mavrikakis, M.; Abbott, N. L. Computational Chemistry-Guided Design of Selective Chemoresponsive Liquid Crystals Using Pyridine and Pyrimidine Functional Groups. *Adv Funct Mater* **2018**, *28* (13), 1703581. https://doi.org/10.1002/adfm.201703581.

(54) Roling, L. T.; Scaranto, J.; Herron, J. A.; Yu, H.; Choi, S.; Abbott, N. L.; Mavrikakis, M. Towards First-Principles Molecular Design of Liquid Crystal-Based Chemoresponsive Systems. *Nat Commun* **2016**, *7*, 13338. https://doi.org/10.1038/ncomms13338.

(55) Szilvási, T.; Roling, L. T.; Yu, H.; Rai, P.; Choi, S.; Twieg, R. J.; Mavrikakis, M.; Abbott, N. L. Design of Chemoresponsive Liquid Crystals through Integration of Computational Chemistry and Experimental Studies. *Chemistry of Materials* **2017**, *29* (8), 3563–3571. https://doi.org/10.1021/acs.chemmater.6b05430.

(56) Daming Cheng; Sridharamurthy, S. S.; Hunter, J. T.; Joon-Seo Park; Abbott, N. L.; Hongrui Jiang. A Sensing Device Using Liquid Crystal in a Micropillar Array Supporting Structure. *Journal of Microelectromechanical Systems* **2009**, *18* (5), 973–982. https://doi.org/10.1109/JMEMS.2009.2029977.

(57) VanTreeck, H. J.; Most, D. R.; Grinwald, B. A.; Kupcho, K. A.; Sen, A.; Bonds, M. D.; Acharya, B. R. Quantitative Detection of a Simulant of Organophosphonate Chemical Warfare Agents Using Liquid Crystals. *Sens Actuators B Chem* **2011**, *158* (1), 104–110. https://doi.org/10.1016/j.snb.2011.05.049.

(58) Hunter, J. T.; Pal, S. K.; Abbott, N. L. Adsorbate-Induced Ordering Transitions of Nematic Liquid Crystals on Surfaces Decorated with Aluminum Perchlorate Salts. *ACS Appl Mater Interfaces* **2010**, *2* (7), 1857–1865. https://doi.org/10.1021/am100165a.

(59) Sen, A.; Acharya, B. R. Alignment of Nematic Liquid Crystals at Inorganic Salt–Liquid Crystal Interfaces. *Liq Cryst* **2011**, *38* (4), 495–506. https://doi.org/10.1080/02678292.2011.553291.

(60) Nayani, K.; Rai, P.; Bao, N.; Yu, H.; Mavrikakis, M.; Twieg, R. J.; Abbott, N. L. Liquid Crystals with Interfacial Ordering That Enhances Responsiveness to Chemical Targets. *Advanced Materials* **2018**, *30* (27), 1706707. https://doi.org/10.1002/adma.201706707.

(61) Nishide, H.; Deguchi, J.; Tsuchida, E. Selective Adsorption of Metal Ions on Crosslinked Poly(Vinylpyridine) Resin Prepared with a Metal Ion as a Template. *Chem Lett* **1976**, *5* (2), 169–174. https://doi.org/10.1246/cl.1976.169.

(62) Belfiore, L. A.; McCurdie, M. P.; Ueda, E. Polymeric Coordination Complexes Based on Cobalt, Nickel, and Ruthenium That Exhibit Synergistic Thermal Properties. *Macromolecules* **1993**, *26* (25), 6908–6917. https://doi.org/10.1021/ma00077a031.

(63) Belfiore, L. A.; McCurdie, M. P. Reactive Blending via Metal-Ligand Coordination. *J Polym Sci B Polym Phys* **1995**, *33* (1), 105–124. https://doi.org/10.1002/polb.1995.090330112.

(64) McCurdie, M. P.; Belfiore, L. A. Spectroscopic Analysis of Transition-Metal Coordination Complexes Based on Poly(4-Vinylpyridine) and Dichlorotricarbonylruthenium(II). *Polymer (Guildf)* **1999**, *40* (11), 2889–2902. https://doi.org/10.1016/S0032-3861(98)00486-8.

(65) Belfiore, L. A.; Pires, A. T. N.; Wang, Y.; Graham, H.; Ueda, E. Transition-Metal Coordination in Polymer Blends and Model Systems. *Macromolecules* **1992**, *25* (5), 1411–1419. https://doi.org/10.1021/ma00031a009.

(66) Yu, S. J.; Pak, K.; Kwak, M. J.; Joo, M.; Kim, B. J.; Oh, M. S.; Baek, J.; Park, H.; Choi, G.; Kim, D. H.; Choi, J.; Choi, Y.; Shin, J.; Moon, H.; Lee, E.; Im, S. G. Initiated Chemical Vapor Deposition: A Versatile Tool for Various Device Applications. *Adv Eng Mater* **2018**, *20* (3), 1700622. https://doi.org/10.1002/adem.201700622.

(67) Baxamusa, S. Conformal Polymer CVD. In *CVD Polymers*; 2015; pp 87–109. https://doi.org/https://doi.org/10.1002/9783527690275.ch5.

(68) Gleason, K. K. Controlled Release Utilizing Initiated Chemical Vapor Deposited (ICVD) of Polymeric Nanolayers. *Front Bioeng Biotechnol* **2021**, *9*, 632753. https://doi.org/10.3389/fbioe.2021.632753.

(69) Tenhaeff, W. E.; McIntosh, L. D.; Gleason, K. K. Synthesis of Poly(4-Vinylpyridine) Thin Films by Initiated Chemical Vapor Deposition (ICVD) for Selective Nanotrench-Based Sensing of Nitroaromatics. *Adv Funct Mater* **2010**, *20* (7), 1144–1151. https://doi.org/10.1002/adfm.200901890.

(70) Petruczok, C. D.; Yang, R.; Gleason, K. K. Controllable Cross-Linking of Vapor-Deposited Polymer Thin Films and Impact on Material Properties. *Macromolecules* **2013**, *46* (5), 1832–1840. https://doi.org/10.1021/ma302566r.

(71) Donadt, T. B.; Yang, R. Amphiphilic Polymer Thin Films with Enhanced Resistance to Biofilm Formation at the Solid–Liquid–Air Interface. *Adv Mater Interfaces* **2021**, *8* (5), 2001791. https://doi.org/10.1002/admi.202001791.

(72) Franklin, T.; Wu, Y.; Lang, J.; Li, S.; Yang, R. Design of Polymeric Thin Films to Direct Microbial Biofilm Growth, Virulence, and Metabolism. *Biomacromolecules* **2021**, *22* (12), 4933–4944. https://doi.org/10.1021/acs.biomac.1c00731.

(73) Roland, C. M. Constraints on Local Segmental Motion in Poly(Vinylethylene) Networks. *Macromolecules* **1994**, *27* (15), 4242–4247. https://doi.org/10.1021/ma00093a027.

(74) Bao, N.; Gold, J. I.; Szilvási, T.; Yu, H.; Twieg, R. J.; Mavrikakis, M.; Abbott, N. L. Designing Chemically Selective Liquid Crystalline Materials That Respond to Oxidizing Gases. *J Mater Chem C Mater* **2021**, *9* (20), 6507–6517. https://doi.org/10.1039/D1TC00544H.

(75) Szilvási, T.; Yu, H.; Gold, J. I.; Bao, N.; Wolter, T. J.; Twieg, R. J.; Abbott, N. L.; Mavrikakis, M. Coupling the Chemical Reactivity of Bimetallic Surfaces to the Orientations of Liquid Crystals. *Mater Horiz* **2021**, *8* (7), 2050–2056. https://doi.org/10.1039/D1MH00035G.

(76) Yu, H.; Szilvási, T.; Wang, K.; Gold, J. I.; Bao, N.; Twieg, R. J.; Mavrikakis, M.; Abbott, N. L. Amplification of Elementary Surface Reaction Steps on Transition Metal Surfaces Using Liquid Crystals: Dissociative Adsorption and Dehydrogenation. *J Am Chem Soc* **2019**, *141* (40), 16003–16013. https://doi.org/10.1021/jacs.9b08057.

(77) Gold, J.; Szilvási, T.; Abbott, N. L.; Mavrikakis, M. Binding of Organophosphorus Nerve Agents and Their Simulants to Metal Salts. *ACS Appl Mater Interfaces* **2020**, *12* (27), 30941–30953. https://doi.org/10.1021/acsami.0c05777.

(78) Frisch, M. J.; Trucks, G. W.; Schlegel, H. B.; Scuseria, G. E.; Robb, M. A.; Cheeseman, J. R.; Scalmani, G.; Barone, V.; Petersson, G. A.; Nakatsuji, H.; Li, X.; Caricato, M.; Marenich, A.; Bloino, J.; Janesko, B. G.; Gomperts, R.; Mennucci, B.; Hratchian, H. P.; Ortiz, J. V.; Izmaylov, A. F.; Sonnenberg, J. L.; Williams-Young, D.; Ding, F.; Lipparini, F.; Egidi, F.; Goings, J.; Peng, B.; Petrone, A.; Henderson, T.; Ranasinghe, D.; Zakrzewski, V. G.; Gao, J.; Rega, N.; Zheng, G.; Liang, W.; Hada, M.; Ehara, M.; Toyota, K.; Fukuda, R.; Hasegawa, J.; Ishida, M.; Nakajima, T.; Honda, Y.; Kitao, O.; Nakai, H.; Vreven, T.; Throssell, K.; J. A. Montgomery, Jr.; Peralta, J. E.; Ogliaro, F.; Bearpark, M.; Heyd, J. J.; Brothers, E.; Kudin, K. N.; Staroverov, V. N.; Keith, T.; Kobayashi, R.; Normand, J.; Raghavachari, K.; Rendell, A.; Burant, J. C.; Iyengar, S. S.; Tomasi, J.; Cossi, M.; Millam, J. M.; Klene, M.; Adamo, C.; Cammi, R.; Ochterski, J. W.; Martin, R. L.; Morokuma, K.; Farkas, O.; Foresman, J. B.; Fox, D. J. Gaussian 09, Revision A.01. Gaussian, Inc.: Wallingford CT 2009.

(79) Perdew, J. P.; Burke, K.; Ernzerhof, M. Generalized Gradient Approximation Made Simple. *Phys Rev Lett* **1996**, *77* (18), 3865–3868. https://doi.org/10.1103/PhysRevLett.77.3865.

(80) Weigend, F.; Ahlrichs, R. Balanced Basis Sets of Split Valence, Triple Zeta Valence and Quadruple Zeta Valence Quality for H to Rn: Design and Assessment of Accuracy. *Physical Chemistry Chemical Physics* **2005**, *7* (18), 3297. https://doi.org/10.1039/b508541a.

(81) Grimme, S.; Antony, J.; Ehrlich, S.; Krieg, H. A Consistent and Accurate Ab Initio Parametrization of Density Functional Dispersion Correction (DFT-D) for the 94 Elements H-Pu. *J Chem Phys* **2010**, *132* (15), 154104. https://doi.org/10.1063/1.3382344.

(82) Zhao, Y.; Truhlar, D. G. The M06 Suite of Density Functionals for Main Group Thermochemistry, Thermochemical Kinetics, Noncovalent Interactions, Excited States, and Transition Elements: Two

New Functionals and Systematic Testing of Four M06-Class Functionals and 12 Other Function. *Theor Chem Acc* **2008**, *120* (1–3), 215–241. https://doi.org/10.1007/s00214-007-0310-x.

(83) Zhang, J. W.; He, G.; Zhou, L.; Chen, H. S.; Chen, X. S.; Chen, X. F.; Deng, B.; Lv, J. G.; Sun, Z. Q. Microstructure Optimization and Optical and Interfacial Properties Modulation of Sputtering-Derived HfO_2 Thin Films by TiO_2 Incorporation. *J Alloys Compd* **2014**, *611*, 253–259. https://doi.org/10.1016/j.jallcom.2014.05.074.

(84) Belfiore, L. A.; Pires, A. T. N.; Wang, Y.; Graham, H.; Ueda, E. Transition-Metal Coordination in Polymer Blends and Model Systems. *Macromolecules* **1992**, *25* (5), 1411–1419. https://doi.org/10.1021/ma00031a009.

(85) Belfiore, L. A.; McCurdie, M. P.; Ueda, E. Polymeric Coordination Complexes Based on Cobalt, Nickel, and Ruthenium That Exhibit Synergistic Thermal Properties. *Macromolecules* **1993**, *26* (25), 6908–6917. https://doi.org/10.1021/ma00077a031.

(86) Belfiore, L. A.; McCurdie, M. P. Reactive Blending via Metal-Ligand Coordination. *J Polym Sci B Polym Phys* **1995**, *33* (1), 105–124. https://doi.org/10.1002/polb.1995.090330112.

(87) Buffeteau, T.; Desbat, B.; Turlet, J. M. Polarization Modulation FT-IR Spectroscopy of Surfaces and Ultra-Thin Films: Experimental Procedure and Quantitative Analysis. *Appl Spectrosc* **1991**, *45* (3), 380–389. https://doi.org/10.1366/0003702914337308.

(88) Wang, L.; Fu, Y.; Wang, Z.; Fan, Y.; Zhang, X. Investigation into an Alternating Multilayer Film of Poly(4-Vinylpyridine) and Poly(Acrylic Acid) Based on Hydrogen Bonding. *Langmuir* **1999**, *15* (4), 1360–1363. https://doi.org/10.1021/la981181+.

(89) Wickenden, A. E.; Krause, R. A. Complexes of Nickel(II) with Acetonitrile. Coordination of Perchlorate. *Inorg Chem* **1965**, *4* (3), 404–407. https://doi.org/10.1021/ic50025a032.

(90) McCurdie, M. P.; Belfiore, L. A. Spectroscopic Analysis of Transition-Metal Coordination Complexes Based on Poly(4-Vinylpyridine) and Dichlorotricarbonylruthenium(II). *Polymer (Guildf)* **1999**, *40* (11), 2889–2902. https://doi.org/10.1016/S0032-3861(98)00486-8.

(91) Nishide, H.; Deguchi, J.; Tsuchida, E. Selective Adsorption of Metal Ions on Crosslinked Poly(Vinylpyridine) Resin Prepared with a Metal Ion as a Template. *Chem Lett* **1976**, *5* (2), 169–174. https://doi.org/10.1246/cl.1976.169.

(92) Wang, L.; Fu, Y.; Wang, Z.; Fan, Y.; Zhang, X. Investigation into an Alternating Multilayer Film of Poly(4-Vinylpyridine) and Poly(Acrylic Acid) Based on Hydrogen Bonding. *Langmuir* **1999**, *15* (4), 1360–1363. https://doi.org/10.1021/la981181+.

(93) Thoen, J.; Cordoyiannis, G.; Glorieux, C. Investigations of Phase Transitions in Liquid Crystals by Means of Adiabatic Scanning Calorimetry. *Liq Cryst* **2009**, *36* (6–7), 669–684. https://doi.org/10.1080/02678290902755564.

(94) Fuller, E. N.; Schettler, P. D.; Giddings, J. C. A New Method for Prediction of Binary Gas-Phase Diffusion Coefficients. *Ind Eng Chem* **1966**, *58* (5), 18–27. https://doi.org/10.1021/ie50677a007.

(95) Hadjichristov, G. B.; Marinov, Y. G.; Petrov, A. G.; Marino, L.; Scaramuzza, N. Dielectric and Electrical Characterization of 5CB Nematic Liquid Crystal Doped with Silver Nanoparticles. *J Phys Conf Ser* **2016**, *682* (1). https://doi.org/10.1088/1742-6596/682/1/012015.

(96) Yang, C.-S.; Lin, C.-J.; Pan, R.-P.; Que, C. T.; Yamamoto, K.; Tani, M.; Pan, C.-L. The Complex Refractive Indices of the Liquid Crystal Mixture E7 in the Terahertz Frequency Range. *Journal of the Optical Society of America B* **2010**, *27* (9), 1866. https://doi.org/10.1364/josab.27.001866.

(97) Baumgärtner, A.; Muthukumar, M. Effects of Surface Roughness on Adsorbed Polymers. *J Chem Phys* **1991**, *94* (5), 4062–4070. https://doi.org/10.1063/1.460656.

(98) Ji, X.; Jie, K.; Zimmerman, S. C.; Huang, F. A Double Supramolecular Crosslinked Polymer Gel Exhibiting Macroscale Expansion and Contraction Behavior and Multistimuli Responsiveness. *Polym Chem* **2015**, *6* (11), 1912–1917. https://doi.org/10.1039/C4PY01715C.

(99) Wrzesińska, A.; Bobowska, I.; Maczugowska, P.; Małolepsza, J.; Błażewska, K. M.; Wypych-Puszkarz, A. Effect of Metal-Ligand Coordination Complexes on Molecular Dynamics and Structure of Cross-Linked Poly(Dimethylosiloxane). *Polymers (Basel)* **2020**, *12* (8), 1680. https://doi.org/10.3390/polym12081680.

(100) Das, M. C.; Bharadwaj, P. K. A Porous Coordination Polymer Exhibiting Reversible Single-Crystal to Single-Crystal Substitution Reactions at Mn(II) Centers by Nitrile Guest Molecules. *J Am Chem Soc* **2009**, *131* (31), 10942–10949. https://doi.org/10.1021/ja9006035.

(101) Beauvais, R. A.; Alexandratos, S. D. Polymer-Supported Reagents for the Selective Complexation of Metal Ions: An Overview. *React Funct Polym* **1998**, *36* (2), 113–123. https://doi.org/10.1016/S1381-5148(98)00016-9.

(102) Yan, Y.; Zhang, J.; Ren, L.; Tang, C. Metal-Containing and Related Polymers for Biomedical Applications. *Chem Soc Rev* **2016**, *45* (19), 5232–5263. https://doi.org/10.1039/C6CS00026F.

(103) Heinke, L.; Wöll, C. Surface-Mounted Metal–Organic Frameworks: Crystalline and Porous Molecular Assemblies for Fundamental Insights and Advanced Applications. *Advanced Materials* **2019**, *31* (26), 1806324. https://doi.org/10.1002/adma.201806324.

Supporting Information

Design of Chemoresponsive Liquid Crystals using Metal-Coordinating Polymer Surfaces

Nanqi Bao,[+] *Tibor Szilvási,*[#] *Trevor Franklin,*[+] *Trenton J. Wolter,*[#] *Ayushi Tripathi,*[+] *Robert J. Twieg,*[$] *Rong Yang,*[*,+] *Manos Mavrikakis,*[*,#] *Nicholas L. Abbott*[*,+]

[+]Smith School of Chemical and Biomolecular Engineering, Cornell University, Ithaca, NY 14853, USA

[#]Department of Chemical and Biological Engineering, University of Wisconsin-Madison, Madison, WI 53706, USA

[$]Department of Chemistry and Biochemistry, Kent State University, 1175 Risman Drive, Kent, Ohio 44242, USA

Additional Computational Details

Figure S1 shows the Neural Anion Model (NAM) of $Ni(ClO_4)_2$ with increasing numbers of pyridine molecules coordinated with the Ni^{2+} ion. The differential binging free energy (ΔG) for the addition of the last pyridine molecule in each case is given in Figure S1. ΔG is negative for the addition of a pyridine molecule up to four pyridine molecules, with exothermicity decreasing as the number of pyridine molecules increases. Because adding the first pyridine group to $Ni(ClO_4)_2$ is more exothermic than adding additional pyridine groups, the **NAM+1Pyr** model is most likely the best model to represent our experimental system, whereby there is a surplus of the metal salt relative to the number of available pyridine groups from the polymer substrate.

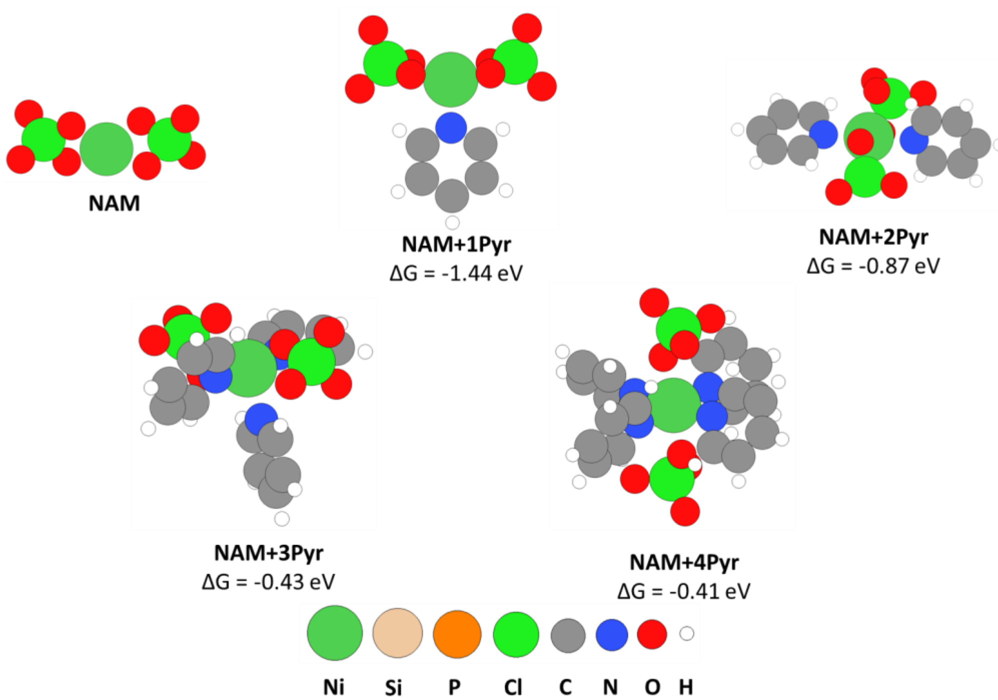

Figure S1. Geometries of the NAM of $Ni(ClO_4)_2$ and the NAM coordinated with one to four pyridine molecules. Differential Gibbs free energies of adsorption for the last pyridine molecules in each case are provided below each energy-optimized structure.

Table S1 shows the binding free energy (G_{BE}) of PhCN and the displacement free energy (G_{DE}) of PhCN by DMMP with each of the five models shown in Figure S1. PhCN binds most strongly to the NAM and generally binds weaker as the number of coordinated pyridine molecules increases. The one exception is that PhCN binds slightly stronger to the NAM+3Pyr model (G_{BE}=-0.15 eV) than to the NAM+2Pyr model (G_{BE}=-0.12 eV). The trend in G_{DE} as the number of coordinated pyridine molecules increases is less clear. The NAM and NAM+2Pyr models have similar G_{DE} values (-0.47 eV and -0.49 eV, respectively), and the NAM+1Pyr and NAM+3Pyr models have similar G_{DE} values (G_{DE}=-0.39 eV and -0.37 eV, respectively). The NAM+4Pyr model has the weakest G_{DE} of -0.29 eV.

Table S1. Calculated G_{BE} of PhCN to $Ni(ClO_4)_2$-plain-(NAM) and to pyridine-coordinated $Ni(ClO_4)_2$ (NAM+nPyr, n=1-4), and calculated G_{DE} of PhCN by DMMP. All values are in eV.

	G_{BE} of PhCN	G_{DE} of DMMP
NAM	-1.04	-0.47
NAM+1Pyr	-0.57	-0.39
NAM+2Pyr	-0.12	-0.49
NAM+3Pyr	-0.15	-0.37
NAM+4Pyr	+0.40	-0.29

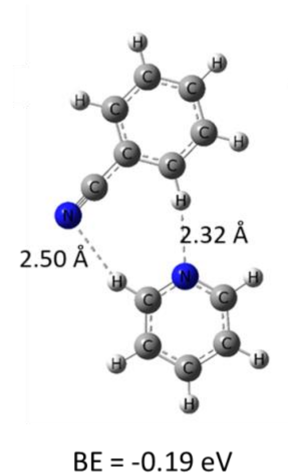

Figure S2. Interaction of PhCN with a pyridine molecule. The binding energy of PhCN to pyridine is -0.19 eV, indicating a weak interaction via hydrogen bonding.

Table S2 shows the G_{BE} of PhCN to the NAM+1Pyr model for several metal perchlorate salts. In the experiments below (Figure S8), 5CB exhibited planar orientations on the P(4VP-*co*-DVB) surfaces decorated with the metal salts highlighted in red (Table S2). $Ni(ClO_4)_2$ (green) is the only metal salt that induced a homeotropic orientation of 5CB on the P(4VP-*co*-DVB) surface, consistent with the calculation prediction for the strongest binding of PhCN to $Ni(ClO_4)_2$ among these metal perchlorate salts.

Table S2. G_{BE} of PhCN to NAM+1Pyr for several metal perchlorate salts. All values are in eV.

NAM+1Pyr	$Fe(ClO_4)_3$	$Al(ClO_4)_3$	$Zn(ClO_4)_3$	$Cu(ClO_4)_2$	$Mn(ClO_4)_2$	$La(ClO_4)_3$	$Ni(ClO_4)_2$
G_{BE} of PhCN	-0.34	-0.38	-0.42	-0.44	-0.46	-0.47	-0.57

Additional Experimental Details

1. Materials

Nickel(II) perchlorate hexahydrate, divinylbenzene (80%), 4-vinylpyridine (95%), and *tert*-butyl peroxide (98%) were purchased from Sigma-Aldrich (Milwaukee, WI). Fischer's Finest glass slides and starch indicator 1% for iodometric titration were purchased from Fischer Scientific (Pittsburgh, PA). Absolute ethanol (anhydrous, 200 proof) was purchased from Pharmco-AAPER (Brookfield, CT). All chemicals and solvents were of analytical reagent grade and were used as received without any further purification. Deionized water possessed a resistivity of at least 18.2 MΩ cm or greater. 5CB was purchased from Jiangsu Hecheng Advanced Materials Co., Ltd (Jiangsu, China). DMMP in nitrogen gas at a concentration of 10 ppm, pure nitrogen gas and pure argon gas were obtained from Airgas (Elmira, NY) and used as received. Silicon wafers for P(4VP-*co*-DVB) characterization were purchased from Pure Wafer (San Jose, CA).

2. Synthesis of polymer thin films

All substrates were sealed in the 25 cm diameter and 5 cm tall reactor chamber, which was evacuated to 4 mTorr by a rotary vane pump (E2M40, Edwards). Divinylbenzene (DVB, Scheme 1c) was heated in a glass jar to 65 °C to produce vapors that were metered into the reactor chamber at 0.25 sccm by a heated mass flow controller (1152C, MKS Instruments). 4-vinylpyridine (4VP, Scheme 1d) was heated in a glass jar to 50 °C to produce vapors that were metered into the reactor chamber at 3.10 sccm by a metering bellows valve (Swagelok). Argon carrier gas and *tert*-butyl peroxide (TBPO, Scheme 1e) were delivered to the reactor at 0.75 and 0.68 sccm, respectively, by mass flow controllers (GE50A, MKS Instruments, Andover, MA). Pressure in the reactor, measured by a capacitance manometer (627B, MKS Instruments, Andover, MA), was then controlled to be 0.4 Torr by a throttle valve (235B, MKS Instruments. Andover, MA). The temperature of the substrate stage was maintained at 25 °C by a recirculating chiller (Thermo Accel 500 LT, Waltham, MA). The deposition was activated by the heating of a filament array (55% Cu/45% Ni, Goodfellow, Pittsburgh PA) positioned 2 cm above the substrate stage to approximately 230 °C by a DC power supply (1715A, B&K Precision, Yorba Linda, CA). Real-time polymer film thickness was monitored with an in situ helium-neon laser (633 nm, JDS Uniphase, San Jose, CA), and depositions were terminated once the P(4VP-*co*-DVB) films (Scheme 1f) reached approximately 200 nm by ceasing all vapor flows, cooling the filament array, and evacuating the reactor chamber.

3. Characterization of P(4VP-*co*-DVB) films

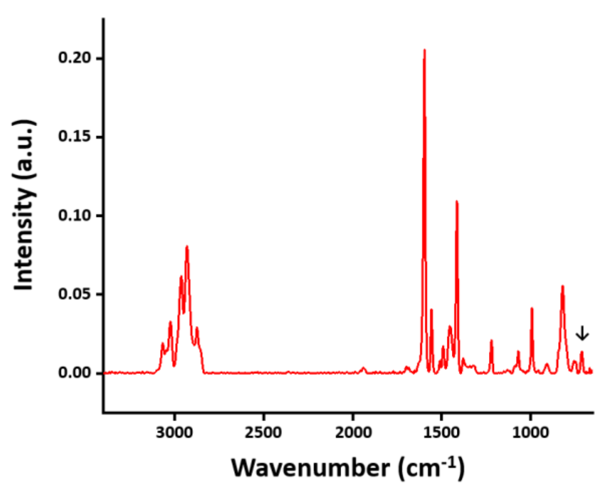

Figure S3. Fourier-transform infrared (FTIR) spectrum of 210 nm-thick P(4VP-*co*-DVB) film using a Bruker VERTEX Series V80v spectrometer in transmission mode. Spectra of films on a Si wafer were collected by using a mercury cadmium telluride detector in the range of 650-3400 cm^{-1} and were background corrected using a bare Si wafer. The area underneath the peak at 710 cm^{-1} corresponding to the C-C vibration in the phenyl moiety of DVB was normalized by the film thickness and compared with the thickness-normalized area under the same peak of a poly(DVB) homopolymer to determine the copolymer composition according to established protocols.[1] Deposition conditions reported in this study yielded a copolymer thin film with 82 mol% 4VP and 18 mol% DVB.

4. Surface density of $Ni(ClO_4)_2$ measured by inductively coupled plasma – optical emission spectrometry (ICP-OES)

To determine the density of metal cation binding sites, metal salts deposited on substrates were dissolved into a 2% nitric acid solution. The concentration of the metal cations in the solution was measured using inductively coupled plasma optical emission spectrometry (ICP-OES, Perkin Elmer 4300). The surface density of the metal salt was calculated from both the ICP-OES data and knowledge of the area of the surface from which the metal salts were extracted. We note that this procedure yields only an apparent density of cation binding sites available to the mesogens, as some cations may be buried within the salt layer on the surface and thus not accessible to mesogens.

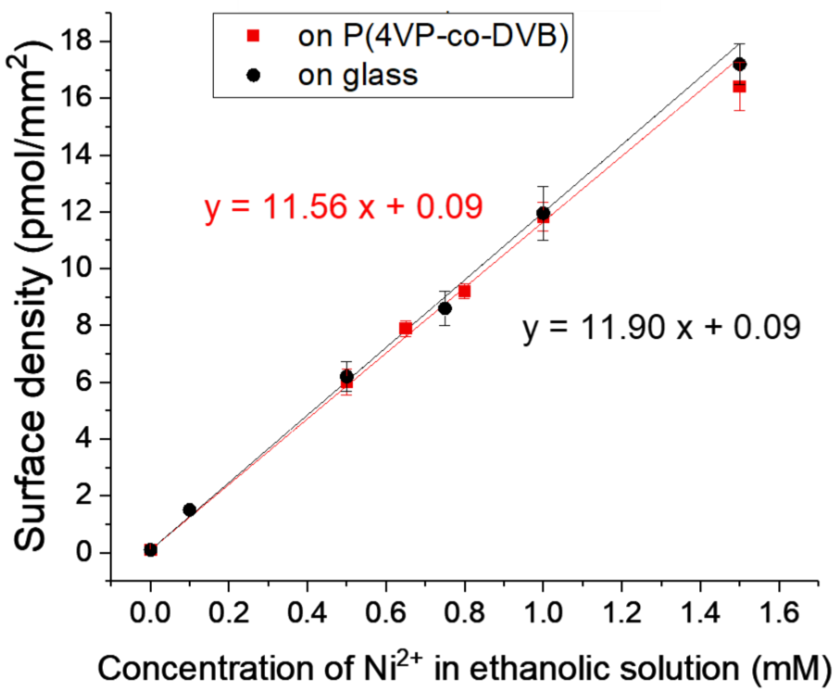

Figure S4. Surface density of Ni^{2+} coated on glass (black) or P(4VP-*co*-DVB) surfaces as a function of its concentration in ethanolic solution as coating solution. These results show that (1) surface density of Ni^{2+} coated on both surfaces varied linearly with the concentration of $Ni(ClO_4)_2$ in the coating solution; (2) this linear relationship (slope) is independent of substrate species.

5. PM-IRRAS of the SiO_2 surface decorated with $Ni(ClO_4)_2$

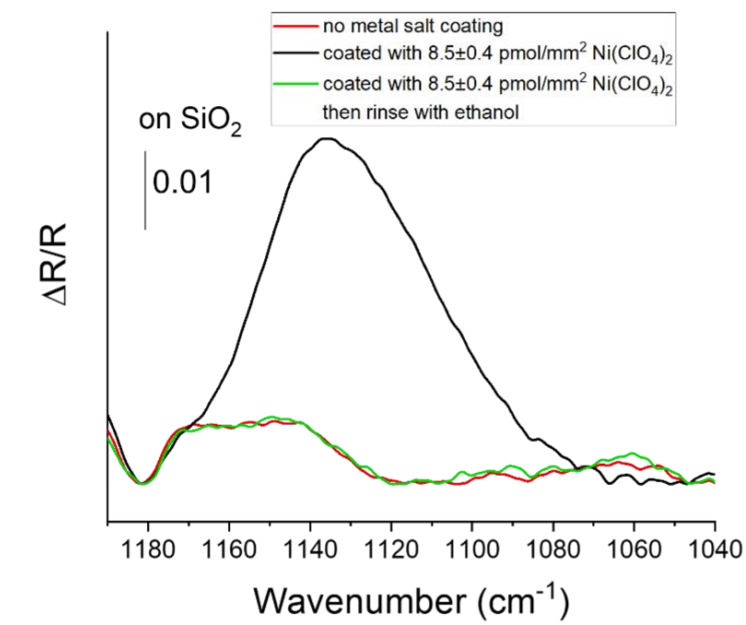

Figure S5. PM-IRRAS of SiO_2 thin films (fabricated by using atomic layer deposition) before (red) and after (black) being decorated with 8.5±0.4 pmol/mm^2 $Ni(ClO_4)_2$, and then being rinsed using ethanol (green). The broad IR peak shown in black corresponds to the vibrational mode for ClO_4^-.[2] The disappearance of the peak in green indicates that $Ni(ClO_4)_2$ was rinsed away from the SiO_2 surface by ethanol, consistent with the computational prediction of the stronger binding of Ni^{2+} to ethanol (G_{BE}=-1.07 eV) as compared to SiO_2 (G_{BE}=-0.94 eV) in Figure 1a.

6. Anchoring of 5CB on the P(4VP-*co*-DVB) surface without $Ni(ClO_4)_2$ coating

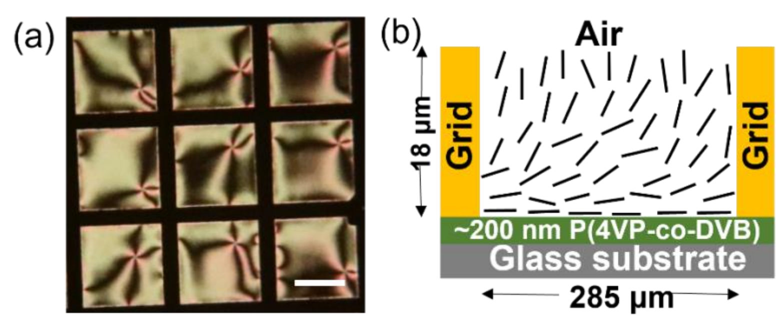

Figure S6. (a) Optical image (crossed polarizers) of 5CB hosted in a copper grid on the P(4VP-*co*-DVB) surface. The scale bars represent 200 µm. (b) Schematic illustration of the director profile (side view) of

5CB in (a). 5CB adopted a tilted/planar orientation on the P(4VP-*co*-DVB) surface due to a weak binding of the nitrile group in 5CB with the pyridine group in P(4VP-*co*-DVB) (Figure S2).

7. Anchoring of 5CB on ethanol-rinsed surfaces

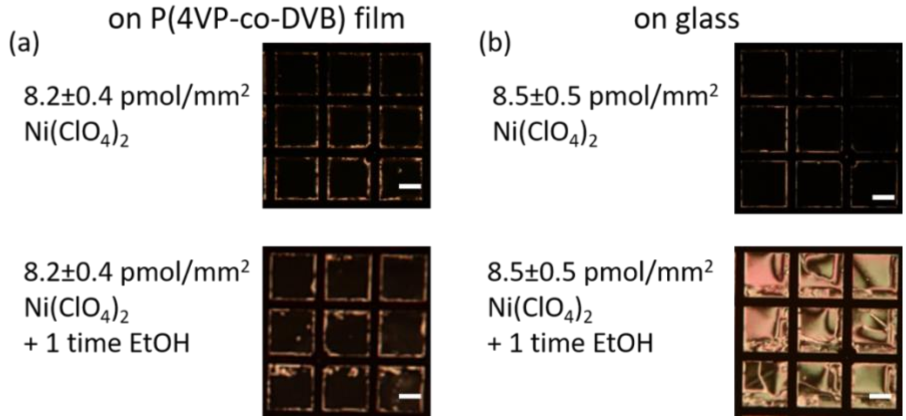

Figure S7. Optical images (crossed polarizers) of 5CB hosted in copper grids on (a) P(4VP-*co*-DVB) surfaces or (b) glass surfaces decorated with ~8 pmol/mm^2 $Ni(ClO_4)_2$ before and after being rinsed using ethanol (prior to deposition of 5CB on surfaces). The scale bars represent 200 µm. These results indicate that a sufficient amount of $Ni(ClO_4)_2$ remained on the P(4VP-*co*-DVB) surface after ethanol rinsing, consistent with the IR results in the main text (Figure 1b). For the glass surface, 5CB adopted a tilted/planar orientation on the ethanol-rinsed surface due to the lack of $Ni(ClO_4)_2$ on the glass surface, consistent with the IR results in Figure S5.

8. Anchoring of 5CB on surfaces decorated with other metal perchlorate salts

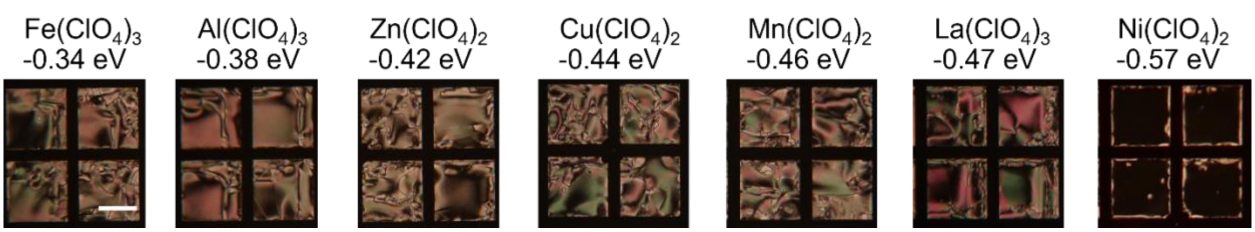

Figure S8. Optical images (crossed polarizers) of 5CB hosted in copper grids on various metal-salt decorated P(4VP-*co*-DVB) surfaces (with surface densities of ~8 pmol/mm^2). The calculated G_{BE}'s of 5CB to metal cations that are coordinated with a pyridine group are listed above images. The scale bars represent 200 µm. These results reveal that homeotropic anchoring of 5CB was observed only for $Ni(ClO_4)_2$ whereas $Fe(ClO_4)_3$, $Al(ClO_4)_3$, $Zn(ClO_4)_2$, $Cu(ClO_4)_2$, $Mn(ClO_4)_2$, and $La(ClO_4)_3$ caused tilted/planar anchoring of 5CB. These results are consistent with our calculation prediction of the strongest binding of PhCN to $Ni(ClO_4)_2$ among these metal perchlorate salts (Table S2).

9. Effect of 4VP-DVB ratio in P(4VP-*co*-DVB) on anchoring of 5CB

In addition to P(4VP-*co*-DVB) films with 82 mol% 4VP, we fabricated P(4VP-*co*-DVB) films with 49 mol% or 0 mol% (pure PDVB) 4VP. For P(4VP-*co*-DVB) with 49 mol% 4VP and pure PDVB samples, DVB (Scheme 1a) was heated in a glass jar to 65 °C to produce vapors that were metered into the reactor chamber at 0.98 and 1.40 sccm, respectively, by a heated mass flow controller (1152C, MKS Instruments). For the sample of P(4VP-*co*-DVB) with 49 mol% 4VP, 4VP (Scheme 1b) was heated in a glass jar to 50 °C to produce vapors that were metered into the reactor chamber at 3.00 sccm by a bellows valve (Swagelok). For the sample of P(4VP-*co*-DVB) with 49 mol% 4VP, the *tert*-butyl peroxide (TBPO, Scheme 1c) and argon flow rates were 0.65 and 0.75 sccm, respectively, and for the PDVB sample they were 0.55 and 0.97 sccm, respectively.

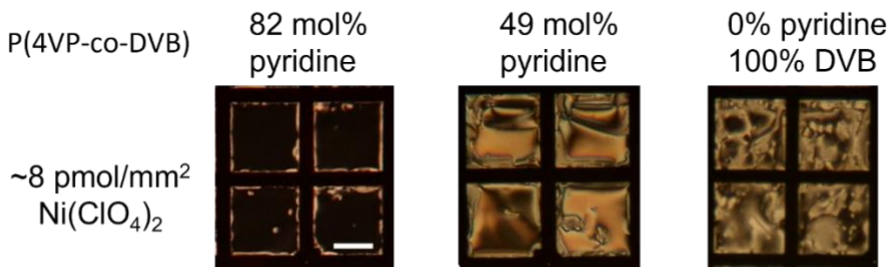

Figure S9. Optical images (crossed polarizers) of 5CB hosted in copper grids on P(4VP-*co*-DVB) surfaces decorated with ~8 pmol/mm^2 $Ni(ClO_4)_2$. The concentration of pyridine in polymer is 82 mol%, 49 mol%, or 0 mol%. We observed tilted/planar orientations of 5CB on the P(4VP-*co*-DVB) surface with 49 mol% pyridine and PDVB (0 mol% pyridine) decorated with ~8 pmol/mm^2 $Ni(ClO_4)_2$. These results indicate that there were no sufficient amounts of $Ni(ClO_4)_2$ at LC-polymer interfaces to induce homeotropic anchoring of 5CB supported on the P(4VP-*co*-DVB) surface with 49 mol% pyridine and the PDVB surface. $Ni(ClO_4)_2$ might be buried in polymers due to the lack of binding (with pyridine) at surfaces. If we assume the surface density of $Ni(ClO_4)_2$ at the LC-polymer interface ($D_{surface}$) to be the product of the overall surface density of $Ni(ClO_4)_2$ (8 pmol/mm^2) and the molar percentage of pyridine in polymer, $D_{surface}$ would be 6.6, 3.9, or 0 pmol/mm^2 for P(4VP-*co*-DVB) surfaces with 82 mol% or 49 mol% pyridine, or the PDVB surface, respectively. From Figure 2b in the main text, we found that the threshold value of $D_{surface}$ for homeotropic anchoring of 5CB is 6.2×82% = 5.1 pmol/mm^2, which is consistent with the observations here. The scale bars represent 200 µm.

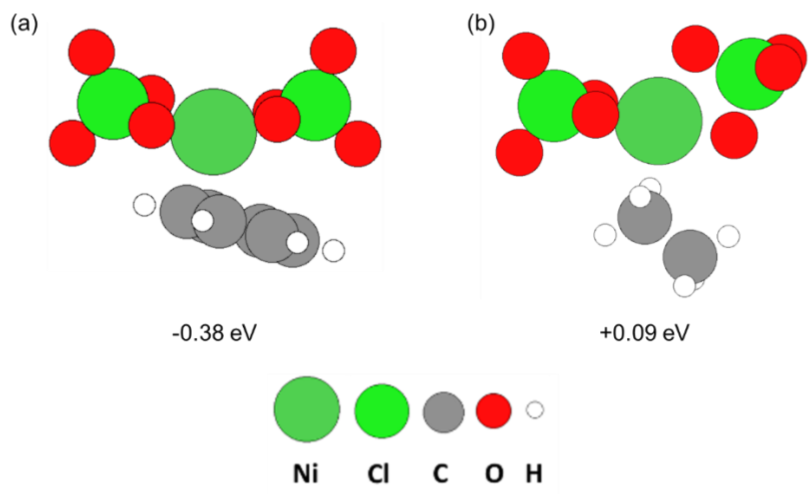

Figure S10. Side view and binding free energy of (a) benzene and (b) ethane each bound to $Ni(ClO_4)_2$. These molecules are used as a surrogate for the phenyl ring and polymer backbone moieties of the polymer chain, respectively. The binding free energies of these two molecules to $Ni(ClO_4)_2$ is sufficiently weak that these moieties are not expected to play a significant role in altering the chemoresponse of this system. For comparison, pyridine binds to $Ni(ClO_4)_2$ with -1.44eV (see fig. S1)

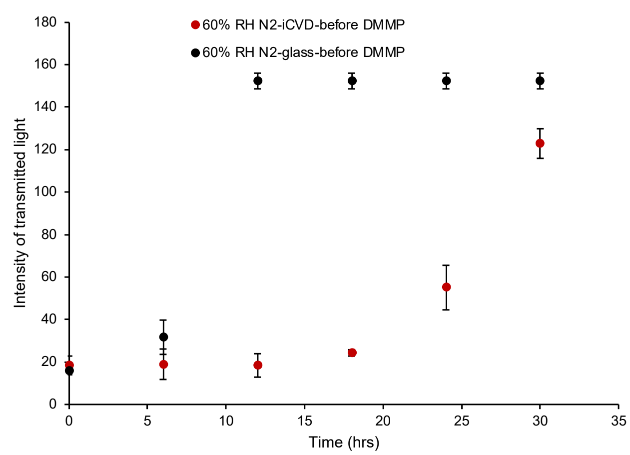

Figure S11. Normalized intensities of polarized light transmitted through 5CB films supported on P(4VP-co-DVB) surfaces decorated with 8.2±0.4 pmol/mm^2 $Ni(ClO_4)_2$ (red) or glass surfaces (black) decorated with 8.5±0.5 pmol/mm^2 $Ni(ClO_4)_2$ during exposure to 60%RH N_2. Inspection of the data reveals that 5CB on the $Ni(ClO_4)_2$-decorated glass surfaces transitioned to a bright optical appearance consistent with a planar anchoring in 14 hrs. This transition is driven by dissolution of metal salt ions into the bulk of LC and occurs even under dry nitrogen as described in Figure 3 of the main manuscript. The latter response of the LC is, therefore, not an adsorbate-induced transition caused by displacement of 5CB by water. DFT calculations shown in Table 2 of the main text indicate that the GDE (displacement free energy) of PhCN by water is approximately -0.14 eV on the pyridine surface. This value of the GDE indicates a thermodynamically favorable displacement of PhCN by water, consistent with experimental observations shown in Figure S11 for 5CB on P(4VP-co-DVB) surfaces.

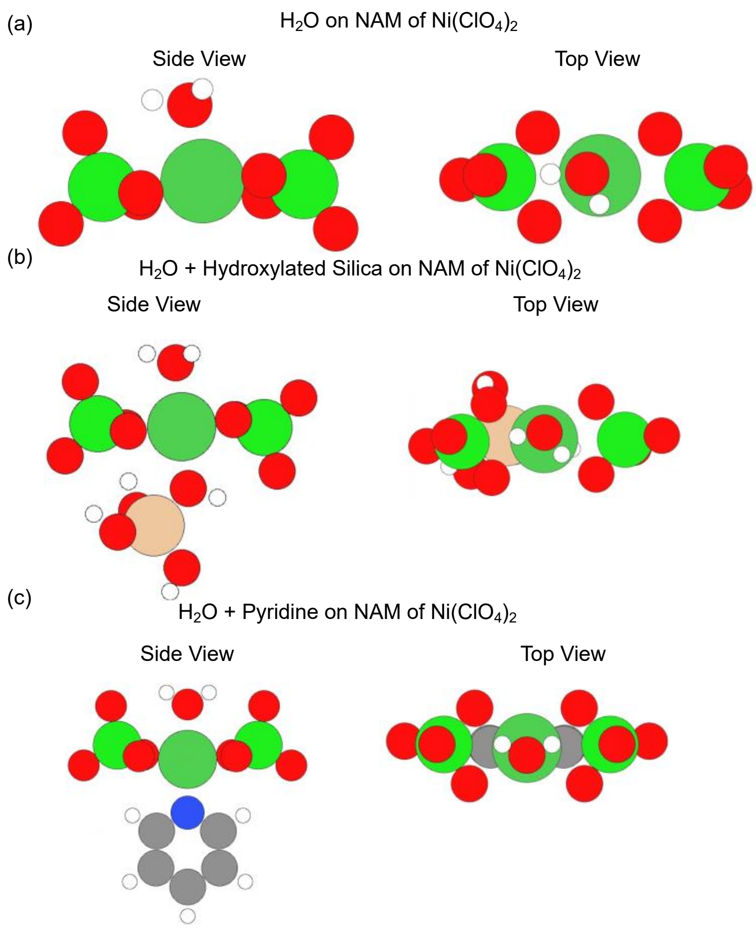

Figure S12. Side view and top view of H_2O bound to (a) NAM of $Ni(ClO_4)_2$ (b) hydroxylated silica on NAM of $Ni(ClO_4)_2$ (c) pyridine on NAM of $Ni(ClO_4)_2$.

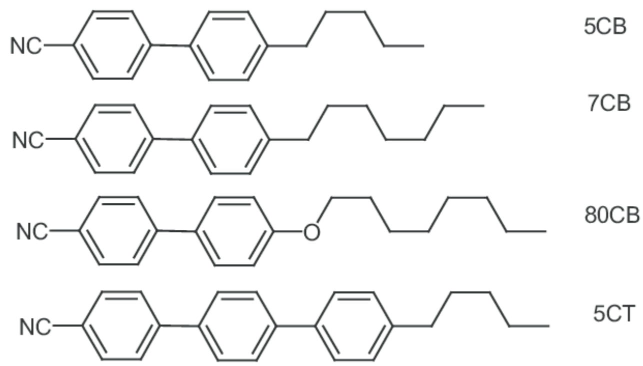

Figure S13. Molecular structure of E7 liquid crystal.

References

(1) Franklin, T.; Wu, Y.; Lang, J.; Li, S.; Yang, R. Design of Polymeric Thin Films to Direct Microbial Biofilm Growth, Virulence, and Metabolism. *Biomacromolecules* **2021**, *22* (12), 4933–4944.

(2) Wickenden, A. E.; Krause, R. A. Complexes of Nickel(II) with Acetonitrile. Coordination of Perchlorate. *Inorg. Chem.* **1965**, *4* (3), 404–407.